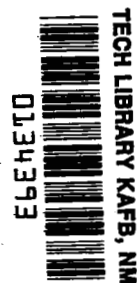


NASA  
TP  
1356  
c.1

# NASA Technical Paper 1356

LOAN COPY: RETURN TO  
AFWL TECHNICAL LIBRARY  
KIRTLAND AFB, N. M.

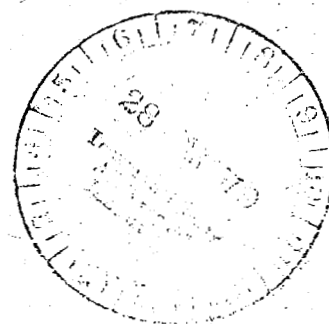


## Pressure and Thermal Distributions on Wings and Adjacent Surfaces Induced by Elevon Deflections at Mach 6

Louis G. Kaufman II and Charles B. Johnson

MARCH 1979

**NASA**





NASA Technical Paper 1356

# Pressure and Thermal Distributions on Wings and Adjacent Surfaces Induced by Elevon Deflections at Mach 6

Louis G. Kaufman II  
*Grumman Aerospace Corporation*  
*Bethpage, New York*

and

Charles B. Johnson  
*Langley Research Center*  
*Hampton, Virginia*



National Aeronautics  
and Space Administration

**Scientific and Technical  
Information Office**

1979

## SUMMARY

Surface pressure distributions and heat transfer distributions were obtained on wing half-models in regions where three-dimensional separated-flow effects are prominent. Unswept and  $50^\circ$ - and  $70^\circ$ -swept semispan wings were tested, for trailing-edge-elevon ramp angles of  $0^\circ$ ,  $10^\circ$ ,  $20^\circ$ , and  $30^\circ$ , with and without cylindrical and flat-plate center bodies and with and without various wing-tip plates and fins. The data, obtained for a free-stream Mach number of 6 and a wing-root-chord Reynolds number of  $18.5 \times 10^6$ , reveal considerably larger regions of increased pressure and thermal loads than would be anticipated using nonseparated flow analyses. For comparable flow conditions, the data and results may be used to guide analyses of wing sweep, elevon deflection angle, and center-body and tip effects on portions of hypersonic airplanes similar to the wing-elevon model described herein.

## INTRODUCTION

Pressure and thermal loads on surfaces of high-speed aircraft can be altered greatly when shock waves impinge on the boundary-layer flows over these surfaces, especially if this causes boundary-layer separation. These interactions are well recognized as an important problem area in the design of high-speed aircraft. Investigations have resulted in an understanding of some features of two-dimensional separated flows (refs. 1 and 2), but there are still many unanswered questions pertaining to three-dimensional flow separation (refs. 3 and 4). The problem has eluded theoretical solution because of its complexity but it is of great practical importance (refs. 1 to 5). An improved understanding of three-dimensional flow separation is needed for the efficient design of high-speed aircraft such as the space shuttle and advanced supersonic transports.

The particular problem addressed herein is flow separation caused by elevon deflections on high-speed aircraft. Even small elevon deflections cause shock waves that can impinge on adjacent fuselage and tip-fin surfaces. The mutual interaction of the shock wave with the boundary layers on these surfaces can result in extensive regions of separated flow and can induce substantial pressure and thermal loads on the surfaces (refs. 3, 4, 6, and 7). These increased loads can compromise an aircraft design. Although these effects are of vital importance to high-speed-aircraft design, there are, unfortunately, very few experimental data of general applicability to three-dimensional separated flows and no satisfactory analytical methods for predicting the interaction effects (refs. 8 to 10).

An experimental program was designed to augment a much needed base of data applicable to turbulent-boundary-layer separation caused by elevon-induced shock waves on high-speed flight vehicles. Fundamental shapes were chosen to make the data as generally applicable as possible and to enhance the usefulness of the data in guiding theoretical analyses of interaction flow regions with

a minimum of extraneous effects. Many geometric parameters were varied to provide data for determining mutual interaction effects of elevon deflection angles, wing sweep, and the presence of tip fins and adjacent fuselage surfaces.

Experiments were conducted in the Langley 20-inch Mach 6 tunnel for wing-root-chord Reynolds numbers of approximately  $18.5 \times 10^6$ . Pressure and heat transfer distributions were obtained, as well as oil-flow and schlieren photographic data, for many model configurations. The purpose of this paper is to present highlights and analyses of the experimental data (refs. 11 and 12), along with some comparisons with theoretical results.

Identification of commercial products in this report is used to adequately describe the model. The identification of these commercial products does not constitute official endorsement, expressed or implied, of such products or manufacturers by the National Aeronautics and Space Administration.

#### SYMBOLS

A	surface area, $\text{cm}^2$
c	specific heat capacity of silicone rubber portions of model, $\text{J/kg}\cdot\text{k}$
g	width of gap between end plate and inboard edge of elevon, cm
HL	hinge line
h	heat transfer coefficient, $\text{W/m}^2\cdot\text{k}$
k	thermal conductivity of silicone rubber portions of model, $\text{W/m}\cdot\text{k}$
M	Mach number
P	ratio of surface pressure to free-stream pressure, $p/p_\infty$
p	pressure, Pa
$R_C$	Reynolds number based on free-stream conditions and length (64.14 cm) of wing root chord
T	temperature, K
t	time, sec
x	streamwise distance measured along either end-plate surface or surface of wing and elevon from wing apex (wing leading edge for unswept wing), cm
y	spanwise distance measured outboard from inboard edge of elevon, cm

$z$	distance measured upward from wing surface, cm
$\gamma$	ratio of specific heats for air (taken as 1.4 herein)
$\epsilon$	elevon deflection angle, deg
$\theta$	elevon shock-wave angle, deg
$\Lambda$	wing sweepback angle, deg
$\rho$	density of silicone rubber portions of model, kg/m <sup>3</sup>

#### Subscripts:

aw	adiabatic wall
i	initial
inv	value calculated for inviscid flow, neglecting separation
l	local undisturbed flow conditions
pc	phase change of paint coating
t	stagnation conditions of free-stream tunnel flow
$\infty$	free-stream flow conditions

### EXPERIMENTAL PROGRAM

#### Model Design Criteria

A wing-elevon portion of a typical high-speed flight configuration was used for testing instead of a particular, complete, winged, flight configuration. The model was used to simulate the wing and aft-fuselage portion of a typical hypersonic flight configuration. (See fig. 1 and refs. 13 to 16.) This approach has the advantage that, for a given test facility, the wing chord for the model can be several times larger than the corresponding wing chord for a complete winged configuration. Therefore, more detailed data may be obtained in the interaction region and, because of the larger wing chord, the root-chord Reynolds number is larger and can be made comparable to those anticipated for flight configurations. The character of the boundary layer, which is particularly important in interaction flow regions (ref. 17), approximates that for full-scale flight vehicles more closely than the flight-configuration model. Along an elevon hinge line on a swept wing, the boundary layer may be characteristically turbulent inboard and laminar outboard (refs. 18 and 19).

## Model Description

In order to investigate wing sweep effects, wings having sweepback angles of  $0^\circ$ ,  $50^\circ$ , and  $70^\circ$  were fabricated (fig. 2). The wings have machined, sharp leading edges ( $11.2^\circ$ ) and a partial-span trailing-edge elevon that can be set at  $0^\circ$ ,  $10^\circ$ ,  $20^\circ$ , or  $30^\circ$  (flow compression) deflection angles. The elevon is sealed to the wing surface to prevent any airflow between the wing and elevon.

The stainless steel model has an end plate (shown in fig. 2) and a cylindrical body (fig. 3) that can be attached to the wings to simulate, in fundamental form, an aft fuselage section. Thus, data may be obtained in the absence of inboard body effects or with an effective inboard end plate by attaching either the end plate or the cylindrical body to the wing. In order to investigate the effects of airflow between an elevon and the aft fuselage section, the end plate may be attached in different spanwise positions on the wings. The resulting gaps between the elevon and the end plate can be varied from zero (end plate sealed to elevon) to 1.27 cm (fig. 2).

Tip fins and plates may also be attached to the model. (See fig. 4.) The tip fins are toed-in, whereas the tip plates are aligned with the free-stream flow direction and are sealed to the elevon to prevent airflow between the tip plate and elevon.

The wings, elevons, and end plate have replaceable inserts. Stainless steel inserts with pressure orifices and tubes are used to obtain pressure data during tunnel runs. These are replaced by silicone rubber inserts to obtain heat transfer data. A photograph of an unswept-wing model with pressure inserts is shown in figure 5. The end plate, large tip plate, and  $30^\circ$  elevon are attached to the wing and sealed for the configuration shown in figure 5. Photographs of a wing-elevon model with inserts used to obtain heat transfer data are shown in figure 6. In these photographs, the cylindrical body and a large tip fin are attached to the  $70^\circ$  wing, and the elevon is deflected  $20^\circ$ . The inserts on the aft portions of the model are composed of 0.64-cm-thick silicone rubber, which is an insulating material well suited for use with the phase-change-paint technique (refs. 20 to 24) for obtaining aerodynamic heat transfer data. The inserts in the fins, plates, body, wing, and elevon encompass the interaction flow region.

## Tunnel and Flow Conditions

The experiments were conducted in the Langley 20-inch Mach 6 tunnel. This is a blowdown wind tunnel with a square test section (appendix of ref. 25). The model is mounted on the strut of an injection system in a chamber directly beneath the tunnel test section (fig. 7).

In order to achieve a high Reynolds number flow, high-stagnation-pressure tunnel operating conditions were chosen for all of the test runs. Nominal values of the stagnation pressure  $p_t$  and temperature  $T_t$  are shown in table I. Also shown are nominal values of the free-stream pressure  $p_\infty$ , Mach number  $M_\infty$ , and the free-stream Reynolds number  $R_C$  based on the wing-root-chord length of 64.14 cm.

TABLE I.- TUNNEL FLOW CONDITIONS

$p_t$ , MPa (psia)	3.56 (516)
$T_t$ , K ( $^{\circ}$ R)	520 (940)
$p_{\infty}$ , kPa (psia)	2.255 (0.327)
$M_{\infty}$	6.00
$R_C$	$18.5 \times 10^6$

The model configurations that were tested are indicated in table II. The wing sweepback angle is  $\Lambda$  and  $\epsilon$  is the elevon deflection angle. Pressure distributions and aerodynamic heat transfer distributions were obtained on the wing, elevon, and end-plate surfaces. The cylindrical body was tested only in combination with the  $70^{\circ}$  wing, and surface pressure distributions were not obtained for this configuration. Profile schlieren flow photographs were taken for all configurations having no inboard attachment. Motion pictures of surface oil flow were taken for all configurations.

TABLE II.- MODEL CONFIGURATIONS\*

$\Lambda$ , deg	Inboard attachment	Outboard attachments
0	None End plate	None, small plate, large plate None, large plate
50	None End plate	None None
70	None End plate Cylinder	None, small plate, small fin None, large plate None, large plate, large fin

\* $\epsilon = 0^{\circ}, 10^{\circ}, 20^{\circ}$ , and  $30^{\circ}$  for all configurations.

#### Test Procedures and Data Reduction

For each tunnel run, the tunnel flow was established before injecting the model into the test position. Strip recorders were used to monitor and record total pressure and total temperature of the tunnel flow during each run. These values varied slightly from run to run but remained essentially constant during each tunnel run.

Differential, multirange, capacitance-type transducers were used to measure the surface pressures. Selected surface pressure orifices were monitored by strip recorders during the pressure tests. When the monitored pressures had stabilized, the surface pressure data were recorded and the model was retracted from the tunnel flow. In order to minimize small discrepancies caused by fluctuations in the tunnel pressure from run to run, the pressures measured on the model surfaces were nondimensionalized using the free-stream static pressure for each tunnel run. The resulting pressure ratios  $P$  are insensitive to minor variations in the tunnel flow pressure from run to run. Repeat tunnel runs for the same configuration revealed that the values of  $P$  repeated to within 0.5 percent. Profile schlieren flow photographs were taken, using a 70-mm film camera, while the surface pressures were being measured.

Surface distributions of aerodynamic heat transfer coefficients were obtained by using the phase-change-paint technique described by Jones and Hunt (ref. 20). The technique makes use of a thin coating of a paint that changes phase (melts) at a known temperature. The model is sprayed with a paint having a specific phase-change temperature and then is quickly injected into the tunnel flow. The model surface temperature rises as a result of aerodynamic heating. In the interaction regions, the paint melts first on the portions of the rubber inserts where the aerodynamic heating rates are greatest. Motion-picture cameras are used to record the progression of the melt line with time. If the initial temperature of the model surface, the adiabatic wall temperature, the phase-change temperature of the paint, and the time the model is exposed to the tunnel flow are known, the local heat transfer coefficient  $h$  at the melt line can be calculated using the transient, one-dimensional, heat conduction equation. A general form of the solution to this equation may be expressed as

$$\frac{h\sqrt{t_{pc}}}{\sqrt{\rho ck}} = f\left(\frac{T_{pc} - T_i}{T_{aw} - T_i}\right) \quad (1)$$

where:  $t_{pc}$  is the time at which the phase change occurs;  $\rho ck$  is the product of thermophysical properties of the model surface material; and  $f$  is a transcendental function of the phase-change temperature  $T_{pc}$ , the initial surface temperature  $T_i$ , and the adiabatic wall temperature  $T_{aw}$ . The function  $f$  has been plotted by Jones and Hunt and is available in reference 20.

In order to obtain reliable values of  $h$ , the phase-change time  $t_{pc}$  should be small compared with the thermal-diffusion time of the model material and large compared with the model-injection time (0.3 sec). The silicone rubber inserts, used for the tunnel runs with phase-change paint, are an insulative material and have a thermal-diffusion time that is much longer than the paint phase-change time. However, because of very high local heating rates for some configurations, the paint melted in these "hot spots" shortly after the model was exposed to the tunnel flow. For this type of heating, the phase-change-paint technique is valuable for ascertaining the precise location of high local heating rates, but the uncertainty in the quantitative value calculated for  $h$  may be quite large (as large as 30 percent for the subject



experiments). However, almost all of the heat transfer data were obtained for model exposure times in excess of 1 second and the uncertainty in the value of  $h$  associated with the error in  $t_{pc}$  is considerably less than 5 percent for these tests. More thorough discussions of the uncertainties inherent in the phase-change-paint technique are available in references 20 to 24.

Values of the adiabatic wall temperature used in equation (1) are calculated for a turbulent-boundary-layer recovery factor (0.896). Oblique shock relations (ref. 26) are used to calculate the inviscid-flow, static-temperature rise across the elevon-generated shock wave. Values of  $T_{aw}/T_t$  calculated in this manner are listed in table III. With possible exceptions near the outboard tip of the 70° wing, large running-length Reynolds numbers justify the assumption of turbulent-boundary-layer flow in the region of interest.

TABLE III.-  $T_{aw}/T_t$  VALUES

$$\left[ T_{aw}/T_t = 0.9089 \text{ on all wing surfaces and on end-plate surface upstream of elevon-generated shock wave} \right]$$

Elevon deflection angle, $\epsilon$ , deg	Value of $T_{aw}/T_t$ on elevon surface and on portion of end-plate surface downstream of elevon-generated shock wave
0	0.9089
10	.9158
20	.9279
30	.9459

The end-plate, wing, and cylindrical-body surfaces were coated with one specified temperature phase-change paint prior to a run. The elevon surface (for  $\epsilon > 0$ ) was sprayed with a higher temperature phase-change paint because of the higher heating rates anticipated on the elevon surface.

Motion-picture cameras were mounted above and on one side of the tunnel test section in order to provide planform and profile motion pictures of the progression of the regions of melted paint on the model. These cameras use 35-mm film and take "double frames" at the rate of 10 per second. Sample frames showing the regression of the phase-change paint on the model surface (70° wing, 30° elevon, cylindrical body, and large tip fin attached) are presented in figures 8 and 9. The regions of melted paint are delineated by dashed lines to aid interpretation of these pictures.

The surface-oil-flow technique was used to ascertain the locations of separation and reattachment on the wing, elevon, and end-plate surfaces.

The silicone rubber inserts were prerubbed with silicone oil (Dow Corning® 550<sup>1</sup> fluid). A random pattern of varying size oil drops was then splattered on the model surfaces using a mixture of 10 ml of the silicone oil, 10 ml of titanium dioxide, and 1 ml of oleic acid. The tunnel flow was started, and the model was injected into the established tunnel flow. The oil flow was observed (TV camera), and top and side motion pictures (10 frames per second) of the oil flow were obtained during the tunnel run. Once the oil-flow pattern was firmly established and there was no further apparent oil droplet movement, the model was retracted from the tunnel flow. (The locations of oil accumulation lines, indicative of flow separation, were observed to be quite steady.) Still photographs of the model were then taken. The length of separated flow ahead of the elevon (as indicated by the oil accumulation line, ref. 19), the apparent location of reattachment on the elevon surface, and the oil-accumulation-line locations on the end plate or cylindrical body were measured directly on the model surfaces after each oil-flow tunnel run.

### Presentation of Experimental Results

The experimental data are presented in references 11 and 12. Sample data are shown here, and the experimental results are summarized. The coordinate system used is shown in figure 10. The streamwise coordinate  $x$  is measured from the wing apex on the surface of the wing and elevon or on the end-plate surface. The spanwise coordinate  $y$  is measured outboard from the inboard edge of the elevon, and the height coordinate  $z$  is measured normal to the plane of the wing.

Pressures measured on the wing, elevon, and end-plate surfaces were divided by the free-stream static pressure for each tunnel run to obtain nondimensional pressure ratios,  $P \equiv p/p_\infty$ . Distributions of the pressure ratios on the wing and elevon surfaces  $P(x,y)$  and on the end-plate surface  $P(x,z)$  are presented as "carpet" plots in reference 11. Sample carpet plots for a 20° elevon on the unswept wing are shown in figures 11 and 12. The values of  $P$  are listed adjacent to the corresponding pressure orifice locations indicated in the figures. In figure 11, the elevon surface is shown and not the projection of the pressure orifice locations in the plane of the wing. Progressing rearward, the surface pressures do not start to increase significantly until just slightly upstream of the elevon hinge line. The elevon—end-plate junction is delineated by the solid line on the end-plate surface (fig. 12). The dotted line indicates the location of the inviscid shock wave for a 20° wedge (ref. 26), and the dash-dot line represents the oil accumulation line evident in a corresponding profile oil-flow photograph (fig. 13).

In addition to surface carpet plots, streamwise distributions of surface pressure ratios, such as those in figure 14, are presented in reference 11. The inviscid value of  $P$  on the elevon surface is that calculated for a 20° wedge in the local flow ( $M_1 = 5.92$ ) over the flat-plate surface. (On the plate surface, the average measured value of  $P = 1.08$  and a free-stream Mach number

---

<sup>1</sup>Dow Corning 550 fluid: Registered tradename of Dow Corning Corporation.

of 6 correspond to a local Mach number flow of 5.92 (refs. 11 and 26).) The schlieren flow photograph corresponding to the 20° elevon on the unswept wing (fig. 15) shows no evidence of separated flow upstream of the elevon hinge line. The apparent thickness of the boundary layer at the hinge line, scaled from schlieren photographs (when there is no appreciable separated flow region), is 0.79 cm.

Heat transfer data in the interaction flow region are presented in reference 12. Tracings of the melt lines on the phase-change paint, from many frames of the motion pictures of a configuration, are superimposed to obtain plots of contours of equal heat-transfer-rate coefficients for the configuration. A sample plot of contours of equal heat-transfer-rate coefficients on the unswept-wing and 20°-elevon surfaces is shown in figure 16. More complex contours, such as those for a 30° elevon on the 70° wing with the cylindrical body and large tip fin attached, are shown in figures 17 and 18. (See ref. 12.) Oil-flow photographs for this configuration (figs. 19 and 20) exhibit oil accumulation lines that demarcate separated-flow regions similar to the extent of increased-heating regions indicated in contour plots of the heat-transfer-rate coefficients.

## DISCUSSION OF RESULTS

Salient aspects of the experimental results are summarized in this section and compared with values calculated using simple analytic methods. Data obtained on the wing and elevon surfaces and the effects of various geometric parameters are described before discussing the data obtained on the end-plate and cylindrical-body surfaces.

### Wing and Elevon Surfaces

Unswept wings.— Pressure-ratio distributions on the unswept-wing and elevon surfaces are shown in figure 21. The distributions are plotted along the streamwise surface coordinate  $x$  at the spanwise station  $y = 8.26$  cm (elevon midspan line). As noted in the previous section, the pressures measured on the wing and the undeflected elevon surfaces are approximately 8 percent larger than the static pressure of the free-stream flow, corresponding to a local Mach number flow over these surfaces of 5.92 (ref. 26). This Mach number and the turning angle  $\epsilon$  are used in oblique shock relations to obtain the inviscid pressure rise on the elevon surface.

The 10° and 20° elevons do not significantly affect the pressure distribution on the wing surface. Pressures on the elevon surface remain below the inviscid values but approach the inviscid value more closely for the 20° elevon than for the 10° elevon. (See fig 21.) Schlieren flow photographs for these configurations indicate shock waves emanating from the elevon hinge line. They show no evidence of flow separation upstream of the hinge line; the apparent boundary-layer thickness at the hinge line is unaffected by either the 10° or 20° elevon (ref. 11). Also, no flow separation is evident in planform oil-flow motion pictures for the 10°- and 20°-elevon configurations.

The pressure-ratio distribution on the wing surface starts to rise approximately 2 cm upstream of the hinge line for the 30° elevon. Characteristic of turbulent-boundary-layer separation (ref. 17), there is a "knee" in the pressure-ratio distribution at the hinge line (fig. 21). The pressure ratios continue to rise, exceed the inviscid value, and attain a maximum value in the vicinity of flow reattachment on the elevon surface. The pressure ratios then decrease and fall below the inviscid value near the elevon trailing edge, presumably because of three-dimensional (finite span) flow effects (ref. 11). Profile schlieren flow photographs and planform oil-flow motion pictures indicate flow separation from the wing surface approximately 2 cm upstream of the hinge line for the 30° elevon. The extent of separated flow is equal to approximately 2.5 times the local undisturbed-flow boundary-layer thickness.

The distribution of heat-transfer-rate coefficients measured on the unswept-wing and undeflected-elevon surfaces along the elevon midspan line is compared with the results of analytical methods in figure 22 (refs. 27 to 30). The method of Anderson and Lewis (ref. 27) gives results that agree with the upstream portion of the experimental data but are about 12 percent above the data near the trailing edge of the end plate. The Van Driest II method for calculating skin friction (ref. 29) is used in the integral method of reference 30 to obtain local heat transfer coefficients. This method agrees with the downstream portion of the data but falls below the upstream portion of the data. The method of Harris (ref. 28) falls between the other two methods and agrees best with the data.

The 10° and 20° elevons do not significantly affect the heating distribution on the wing surface upstream of the hinge line, but the heating distributions on the elevon surfaces are substantially different (fig. 23). The heat-transfer-rate coefficient is nearly constant along the midspan line of the 10° elevon, whereas the highest heating on the 20° elevon occurs near the trailing edge. These experimental distributions are compared with ones calculated using the Van Driest II theoretical method (described in refs. 29 and 30) by assuming a virtual origin at the elevon hinge line and using the measured pressure distributions for the 10° and 20° elevons. Experiment and theory agree for the 10° elevon but differ substantially for the 20° elevon. We attribute this difference to the substantial thickening of the boundary layer downstream of the hinge line, which is not accounted for adequately in the theory. Distributions of heat-transfer-rate coefficients on the elevon surfaces depend strongly on the upstream boundary layer, on the elevon deflection angle, and on several other geometric parameters (ref. 12).

The 30° elevon causes the flow to separate from the wing surface upstream of the hinge line. This results in generally higher heating than expected over the wing surface, which cannot be attributed to an increase in pressure. (See refs. 11 and 12.) The reason for this increase in heating level on the wing with a 30° elevon is not understood. Separation also results in very large heat transfer coefficients on the elevon surface (fig. 24). The largest heat transfer coefficients on the elevon surface correspond to the location (apparent in profile schlieren flow photographs (ref. 11)) where there is a local thinning (necking down) of the viscous flow in the region of reattachment on the elevon surface. Again, the experimental distribution is compared with that calculated

using the Van Driest II theory assuming a virtual origin at the hinge line and using the measured pressure distribution on the 30° elevon (refs. 29 and 30). The measured heat-transfer-rate coefficients are considerably higher at reattachment of the boundary layer than those calculated theoretically, due in this case to the thinning of the boundary layer in the region of reattachment on the elevon surface. In all cases, the experimental distributions approach the theoretical ones far downstream of the hinge line (figs. 23 and 24).

Wing-sweep effect.— Wing sweepback has little effect on the surface pressure distributions but substantial effect on the surface heat-transfer-coefficient distributions. Examination of oil-flow motion pictures reveals streamwise flow on the wing and elevon surfaces with no separation for  $\epsilon = 0^\circ$ ,  $10^\circ$ , or  $20^\circ$  on the swept wings or on the unswept wing. However, wing sweep has some effect on the extent of flow separation ahead of the 30° elevon. Wing-sweep effects on the locations of the oil accumulation lines are indicated in figure 25. The effects are negligible except near the outboard portion of the 70° wing. The boundary layer is thinner in this region which results in a shorter extent of separated flow. The data shown in reference 11 indicate that, for the swept wings, the streamwise increase in pressure on the wing and elevon surfaces, in the vicinity of the hinge lines, is steeper along the outboard line of pressure orifices ( $y = 14.45$  cm) than along the inboard lines of pressure orifices. The pressure gradient ( $dp/dx$ ) along the outboard line of orifices is steepest for the 30° elevon attached to the 70° wing (ref. 11).

The additional loads on the wing surface caused by flow separation ahead of the 30° elevon were calculated by integrating the measured pressure distributions and are listed as nondimensional ratios in table IV. The area of

TABLE IV.— INCREASED LOAD ON WING IN REGION OF FLOW SEPARATION

[ Ratios of load in region extending 2.5 cm upstream of  
30°-elevon hinge line to load in same region for  
undisturbed flow ]

Attachments	$\Lambda = 0^\circ$	$\Lambda = 50^\circ$	$\Lambda = 70^\circ$
None	2.01	2.02	1.98
Large tip plate	2.15		
End plate (1.27-cm gap*)	2.12		
End plate (0.64-cm gap)	2.14		2.07
End plate	2.16	2.15	2.09
End plate (1.27-cm gap) and large tip plate			2.07
End plate (0.64-cm gap) and large tip plate			2.12
End plate and large tip plate	2.21		2.10

\*Gap size is spanwise space between end plate and elevon.

integration was consistently taken as the region extending 2.5 cm upstream of the hinge line. The pressure rise on the wing surface, caused by flow separation, is contained within this region for all pressure instrumented configurations. The ratios listed in table IV are the values of the pressure ratios  $P$  integrated over the region, divided by the integral of the pressure-ratio distribution for undisturbed flows  $P_1$  over the same region:

$$\frac{\int P \, dA}{\int P_1 \, dA}$$

Perusal of the values listed in this table shows that wing sweep has a small effect on the load induced on the wing surface. The load on the wing surface is increased only when there is flow separation ( $\epsilon = 30^\circ$ ); there is no additional load on the wing without separation ( $\epsilon = 0^\circ, 10^\circ, \text{ or } 20^\circ$ ).

Pressure-ratio distributions measured on the elevon surface were integrated to obtain the force normal to the elevon surface. This force was divided by the integral over the elevon surface area of the pressure ratio calculated by inviscid-flow analyses (fig. 21) to obtain the ratios listed in

table V:  $\frac{\int P \, dA}{\int P_{inv} \, dA}$ . The measured loads are less than those calcu-

lated using inviscid-flow analyses. Again, wing sweep has little effect on the total load on the elevon.

Contours of equal heat transfer coefficients parallel the wing leading edges (fig. 26). The contours on the wing surfaces are insensitive to elevon deflections and remain parallel to the leading edges upstream of the region of increased heating induced by deflected elevons (ref. 12). Heating distributions on the deflected elevon surfaces, however, are strongly affected by wing sweepback. (See ref. 12.) Sample contours (fig. 27) show that the heat transfer to  $30^\circ$ -elevon surfaces is somewhat reduced for the  $50^\circ$  wing but that the distribution is similar to that for the unswept wing. However, the heating on the  $30^\circ$ -elevon surface is substantially reduced and the heating distribution is significantly altered when the elevon is attached to the  $70^\circ$  wing. The heating is no longer symmetric about the elevon midspan line but is generally greater outboard than inboard (fig. 27). For both the unswept wing and the  $50^\circ$  swept wing, the boundary layer is turbulent at the hinge-line station across the span of the wing. For the  $70^\circ$  swept wing the boundary layer at the hinge-line station is turbulent inboard but laminar outboard (ref. 19).

Center and tip body effects.— For  $\epsilon < 30^\circ$  (no flow separation), the end plate and the tip plate have negligible effects on the streamwise nature of the surface flow and on the pressure distributions on the wing surface (ref. 11). However, the end and tip plates prevent the spanwise drop-off in pressure on the inboard and outboard portions, respectively, of the elevon surface. This effect is most pronounced near the trailing edge of the  $30^\circ$  elevon. With no end plate for example, the pressure on the inboard portion of the  $30^\circ$ -elevon surface is 5 to 10 percent less than the pressure on the middle portion of the elevon surface. The end plate prevents this drop-off in surface pressure.

The end and tip plates also prevent spanwise venting of the vortical separated flow upstream of the  $30^\circ$  elevon and result in a more nearly uniform

TABLE V.- RATIOS OF MEASURED TO THEORETICAL (INVISCID FLOW)  
LOADS ON ELEVON SURFACE

Attachments	$\Lambda = 0^\circ$	$\Lambda = 50^\circ$	$\Lambda = 70^\circ$
$\epsilon = 10^\circ$			
None	0.815		0.836
End plate	.815		.841
$\epsilon = 20^\circ$			
None	0.882	0.876	0.889
End plate	.900	.890	.897
End plate (0.64-cm gap*) and large tip plate			.919
End plate and large tip plate	.901		.923
$\epsilon = 30^\circ$			
None	0.888	0.886	0.882
Large tip plate	.900		
End plate (1.27-cm gap*)	.901		
End plate (0.64-cm gap)	.904		
End plate	.906	.904	.904
End plate (1.27-cm gap) and large tip plate			.908
End plate (0.64-cm gap) and large tip plate			.914
End plate and large tip plate	.911		.920

\*Gap size is spanwise space between end plate and elevon.

extent of separation (fig. 28). For the subject test conditions, the elevon aspect ratio is sufficiently large so that the inboard and outboard pressure distributions are independent of one another. As evidenced in tables IV and V, the end plate and tip plate have relatively little effect on either the load induced on the wing surface or the load on the elevon surface. Leaving a gap between the end plate and the elevon diminishes the effectiveness of the end plate in preventing the inboard drop-off in pressure on the elevon surface and in preventing inboard venting of the separated flow upstream of the 30° elevon (ref. 11).

As indicated in figure 29, replacing the end plate with the cylindrical body greatly distorts the oil accumulation line (which indicates separation) and more than doubles the maximum extent of separation upstream of the elevon (to approximately 5 cm). The complexity of the surface flow in the separation region is evident in the frame from the planform oil-flow motion picture shown in figure 19. Although the shock wave emanating from the cylindrical body greatly distorts the separated flow ahead of the 30° elevon, it has little effect on the nonseparated-surface-flow streamlines ahead of the 20° elevon (cf figs. 19 and 30).

The only significant effect the end plate and tip plate have on the heat transfer distribution on the wing surface is the slightly larger region of separated flow with its concomitant higher heating rate (turbulent separation). However, the end plate and tip plate can substantially alter the heat transfer distribution on the surface of a deflected elevon. Attaching the tip plate generally results in increased heating on the outboard portion of deflected elevon surfaces. The region of increased heating is limited to the outboard 20 percent or less of the elevon span. The extent of the region is reduced when the large tip plate is replaced by the large tip fin and is further reduced when either the small tip plate or small tip fin are used (ref. 12).

The shock wave from the cylindrical body results in streaks of relatively high heat transfer on the inboard portion of the 70° wing (figs. 31 and 32). The areas of high heating on the elevon surface occur on the inboard portion (near the cylindrical body) and in a region just aft of the elevon hinge line. However, the maximum values of the heat transfer coefficient on the 10°, 20°, and 30°-elevon surfaces are reduced when the cylindrical body is attached to the 70° wing. The maximum values on the 20°- and 30°-elevon surfaces are less when the cylindrical body is attached than when the end plate is attached to the 70° wing.

#### End-Plate and Cylindrical-Body Surfaces

The extent of increased pressure and heating on the end-plate surface, caused by deflected elevons, is demarcated fairly well by the oil accumulation lines apparent in profile oil-flow motion pictures (fig. 13). Once the surface oil-flow pattern becomes established, the location of the oil accumulation line remains quite steady during the remainder of the tunnel run. Locations of these lines, for the three different elevon deflection angles, are plotted in figure 33. The loci of the elevon surface and the shock wave location calculated for inviscid flow (ref. 26) are also shown in the figure. The regions of



disturbed flow on the end-plate surface, as delineated by the oil accumulation lines, are far larger than would be anticipated using inviscid-flow analyses. Furthermore, the surface flow downstream of the oil accumulation line nearly parallels this line and not the line formed by the elevon surface. The oil accumulation lines on the end-plate surface are unaffected by wing sweep; they are the same for  $\Lambda = 0^\circ$ ,  $50^\circ$ , or  $70^\circ$ .

Streamwise pressure-ratio distributions on the end-plate surface are plotted in figure 34. These distributions are independent of wing sweep-back angle. Different height (z) stations are used for each elevon deflection angle in order to obtain a relatively large streamwise distance from the oil accumulation line to the intercept with the elevon surface. (See sketch of flow in fig. 34.) The inviscid-flow values shown are those corresponding to two-dimensional flow over a wedge. (See fig. 21 and ref. 26.) The pressures start to rise far upstream of the inviscid-shock location. For the larger elevon deflection angles, the pressure distributions on the end-plate surface strongly resemble those for turbulent flow separation (refs. 7, 17, and 31). The knees in the present distributions occur at the inviscid-shock location. In general, the pressure induced on the end-plate surface is less than that measured on the elevon surface. For the  $30^\circ$  elevon however, the pressure on the end-plate surface in the vicinity of the elevon exceeds that measured directly on the elevon surface (cf figs. 21 and 34).

The side force induced on the end-plate surface is less than would be calculated using two-dimensional inviscid-flow analyses. Ratios of loads induced on the end-plate surface to those calculated using two-dimensional inviscid-flow analyses are listed in table VI. The integrated, measured pressure loads

TABLE VI.- RATIOS OF MEASURED TO THEORETICAL (TWO-DIMENSIONAL  
INVISCID-FLOW) LOADS INDUCED ON END-PLATE  
SURFACE BY DEFLECTED ELEVONS

$\epsilon$ , deg	Gap size,* cm	$\Lambda = 0^\circ$	$\Lambda = 50^\circ$	$\Lambda = 70^\circ$
10	0	0.90		0.90
20	0	0.85	0.87	0.87
20	.64			.37
30	0	0.91	0.95	0.98
30	.32	.48		.50
30	.64	.52		.52
30	.95	.26		.27
30	1.27	.17		.17

\*Gap size is spanwise space between end plate and elevon.

$\left( \oint (p - p_1) dA \right)$  are less than those calculated using two-dimensional inviscid-flow analyses  $((p_{inv} - p_1)A_{inv})$ , even though the area of the increased pressure is larger. The addition of a tip plate has no effect on the induced load, and wing sweep has only a small effect on the elevon-induced load on the end-plate surface.

Leaving a gap between the end plate and elevon reduces the load induced on the end-plate surface (see table VI) and reduces the extent of disturbed flow on the end-plate surface upstream of the intercept with the plane of the elevon surface. On the elevon-shaded area of the end-plate surface (within the gap), the pressure ratios diminish from large values near the locus of the elevon intercept to near unity (ref. 11). Average pressure ratios measured on the portion of the end-plate surface shaded by the elevon are listed in table VII.

TABLE VII.- AVERAGE PRESSURE RATIO  $P$  VALUE ON END-PLATE  
SURFACE IN GAP REGION BETWEEN END PLATE AND ELEVON

$\epsilon$ , deg	Gap size,* cm	$\Lambda = 0^\circ$	$\Lambda = 70^\circ$
20	0.64		2.81
30	0.32	2.89	3.00
30	.64	3.21	2.96
30	.95	3.21	3.51
30	1.27	3.37	3.40

\*Gap size is spanwise space between end plate and elevon.

Lines of constant heat-transfer-rate coefficients, upstream of the elevon-induced interaction region, parallel the leading edge of the end plate (figs. 35 and 36) and are the same whether the end plate is attached to the unswept,  $50^\circ$ , or  $70^\circ$  wings. Similar to the effects on oil-accumulation-line locations and on the pressure distributions, gaps between the end plate and elevon result in smaller regions of increased heating on the end-plate surface. Neither wing sweepback nor the addition of tip fins have any noticeable effect on the heating distributions on the end-plate surface. However, the general level of heating on the end-plate surface upstream of the interaction region is larger for the  $30^\circ$  elevon than for the  $10^\circ$  and  $20^\circ$  elevons. As was previously noted for the wing (with the  $30^\circ$  elevon), the reason for the higher heating upstream of the disturbance caused by the  $30^\circ$  elevon is not understood. The  $10^\circ$  and  $20^\circ$  elevons do not affect the end-plate heating distribution upstream of the interaction region (cf figs. 35 and 36). For all elevon deflection angles, the highest

heating rates occur adjacent to the intercept of the plane of the elevon surface with the end plate.

Lines of constant heat-transfer-coefficient contours on the cylindrical body parallel the ridge line of the body (ref. 12). An oil accumulation line occurs at the shoulder of the body, where the cylinder joins the planar portion of the body. The surface flow on the cylindrical body, when there are no elevon deflections, resembles that on a blunt-leading-edge wing. With deflected elevons, the limiting line of the interaction region on the cylindrical body curves downstream (ref. 12). The maximum heating on the body is comparable to that on the end plate when there is a gap; it is less than the maximum heating on the end plate when there is no gap (ref. 12). The addition of tip fins does not affect the heating distribution on the body surface.

### CONCLUSIONS

Data obtained on basic configurations for which there are important three-dimensional separated-flow effects, that cannot be predicted using current theoretical methods, are described. The configurations are representative of the fuselage—wing—elevon portions of hypersonic aircraft. The data, obtained for Mach 6 flows and a wing-root-chord Reynolds number approximately  $18.5 \times 10^6$ , can be used to guide analyses of flap- or elevon-induced heating on adjacent surfaces of hypersonic aircraft for similar geometries and flow conditions.

Pressures and heating rates on the wing surfaces are unaffected by  $10^\circ$  and  $20^\circ$  elevon deflections. For the subject flow conditions, typically turbulent separation occurs upstream of  $30^\circ$  elevons; pressures and heating rates on the wing surface are increased in the separated flow region. The end plate and tip plate have relatively little effect on the extent of the separated flow region; they tend to make the separated flow region more nearly two-dimensional. The cylindrical body, however, strongly affects the separated flow region, making it more extensive and highly asymmetric.

Pressure loads on the elevon surfaces are considerably smaller than those calculated using inviscid-flow analyses. Wing sweepback and tip fins have relatively little effect on the pressure distributions, but strongly affect the heating distributions on the elevon surfaces.

The elevons induce increased pressures and heating rates on the adjacent end-plate or cylindrical-body surfaces over regions that are much more extensive than would be anticipated using inviscid-flow analyses. However, the total side force induced on the end plate is less than anticipated.

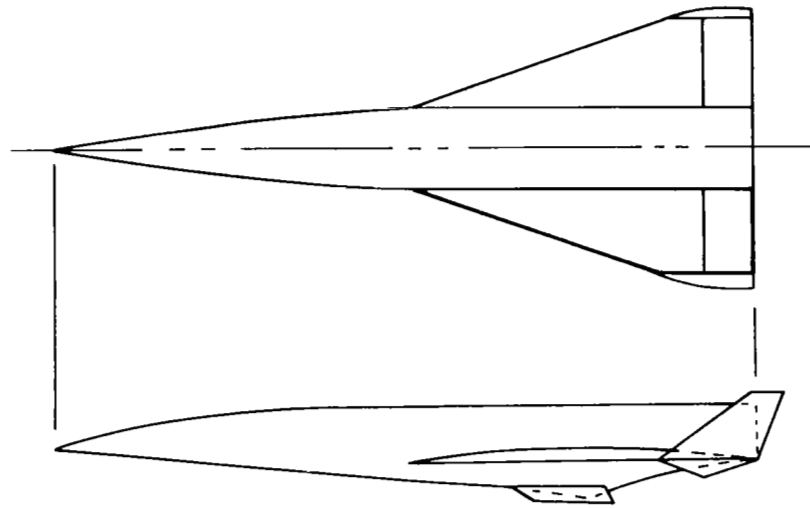
Langley Research Center  
National Aeronautics and Space Administration  
Hampton, VA 23665  
December 15, 1978

## REFERENCES

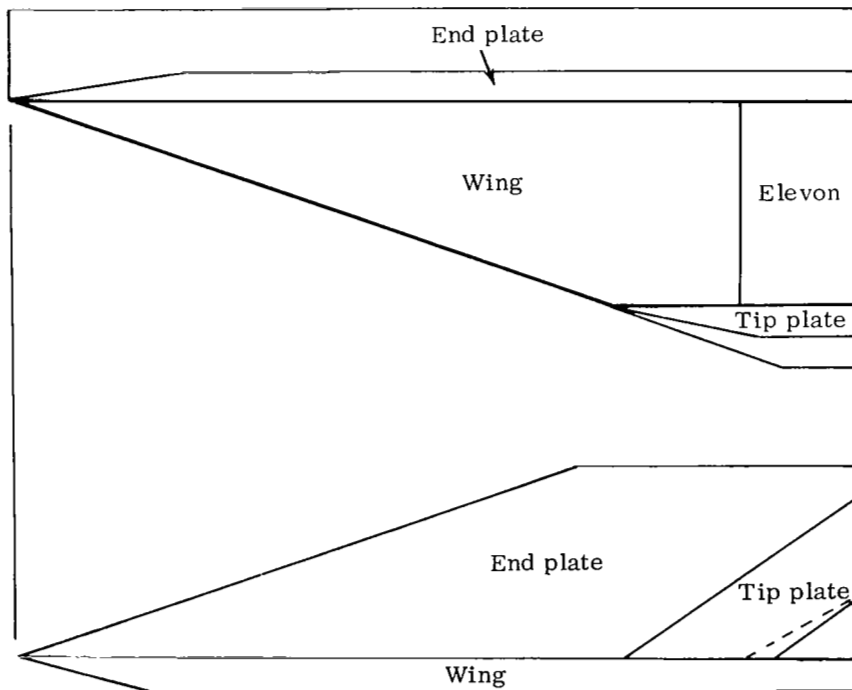
1. Korkegi, Robert H.: Survey of Viscous Interactions Associated With High Mach Number Flight. AIAA J., vol. 9, no. 5, May 1971, pp. 771-784.
2. Ryan, B. M.: Summary of the Aerothermodynamic Interference Literature. Tech. Note 4061-160, Naval Weapons Center (China Lake, Calif.), Apr. 1969.
3. Goldberg, Theodore J.: Three-Dimensional Separation for Interaction of Shock Waves With Turbulent Boundary Layers. AIAA J., vol. 11, no. 11, Nov. 1973, pp. 1573-1575.
4. Schepers, H. J.: Flow and Heat Transfer Measurements in Corner Regions at Hypersonic Speeds. ESA TT-302, 1976. (Available from NTIS.)
5. Sedney, Raymond; and Kitchens, Clarence W., Jr.: The Structure of Three-Dimensional Separated Flows in Obstacle, Boundary-Layer Interactions. Flow Separation, AGARD-CP-168, Nov. 1975, pp. 37-1 - 37-15.
6. Korkegi, R. H.: Comparison of Shock-Induced Two- and Three-Dimensional Incipient Turbulent Separation. AIAA J., vol. 13, no. 4, Apr. 1975, pp. 534-535.
7. McCabe, A.: The Three-Dimensional Interaction of a Shock Wave With a Turbulent Boundary Layer. Aeronaut. Q., vol. XVII, pt. 3, Aug. 1966, pp. 231-252.
8. Peake, David J.; Rainbird, William J.; and Atraghji, Edward G.: Three-Dimensional Flow Separations on Aircraft and Missiles. AIAA J., vol. 10, no. 5, May 1972, pp. 567-580.
9. Whitehead, Allen H., Jr.; Sterrett, James R.; and Emery, James C.: Effects of Transverse Outflow From a Hypersonic Separated Region. AIAA J., vol. 10, no. 4, Apr. 1972, pp. 553-555.
10. Small, William J.; Kirkham, Frank S.; and Fetterman, David E.: Aerodynamic Characteristics of a Hypersonic Transport Configuration at Mach 6.86. NASA TN D-5885, 1970.
11. Kaufman, Louis G., II; and Johnson, Charles B.: Pressure Distributions Induced by Elevon Deflections on Swept Wings and Adjacent End-Plate Surfaces at Mach 6. NASA TM X-3470, 1977.
12. Johnson, Charles B.; and Kaufman, Louis G., II: Heat Transfer Distributions Induced by Elevon Deflections on Swept Wings and Adjacent Surfaces at Mach 6. NASA TM-74045, 1978.
13. Hypersonic Aircraft by 2000 Pushed. Aviation Week & Space Technol., vol. 99, no. 12, Sept. 1973, pp. 52-57.

14. Clark, Louis E.; and Richie, Christine B.: Aerodynamic Characteristics at Mach 6 of a Hypersonic Research Airplane Concept Having a 70° Swept Delta Wing. NASA TM X-3475, 1977.
15. Creel, Theodore R., Jr.; and Penland, Jim A.: Low-Speed Aerodynamic Characteristics of a Hypersonic Research Airplane Concept Having a 70° Swept Delta Wing. NASA TM X-71974, 1974.
16. Nagel, A. L.; and Becker, J. V.: Key Technology for Airbreathing Hypersonic Aircraft. AIAA Paper No. 73-58, Jan. 1973.
17. Chapman, Dean R.; Kuehn, Donald M.; and Larson, Howard K.: Investigation of Separated Flows in Supersonic and Subsonic Streams With Emphasis on the Effect of Transition. NACA Rep. 1356, 1958.
18. Whitehead, Allen H., Jr.; and Keyes, J. Wayne: Flow Phenomena and Separation Over Delta Wings With Trailing-Edge Flaps at Mach 6. AIAA J., vol. 6, no. 12, Dec. 1968, pp. 2380-2387.
19. Kaufman, Louis G., II; and Freeman, L. Michael: Separation Ahead of Controls on Swept Wings. ARL TR 75-0134, U.S. Air Force, June 1975.
20. Jones, Robert A.; and Hunt, James L.: Use of Fusible Temperature Indicators for Obtaining Quantitative Aerodynamic Heat-Transfer Data. NASA TR R-230, 1966.
21. Kaufman, Louis G., II; Leng, Jarvis; and Johnson, Arnold R.: Exploratory Tests Using Temperature-Sensitive Paints To Obtain Hypersonic Heat Transfer Data on Spheres and on Fin-Plate Models. RM-487, Grumman Aerospace Corp., Sept. 1970.
22. Hunt, James L.; and Jones, Robert A.: Heating and Flow-Field Studies on a Straight-Wing Hypersonic Reentry Vehicle at Angles of Attack From 20° to 80° With Simulation of Real-Gas Trends. NASA TN D-7108, 1973.
23. Maise, George; and Rossi, Michael J.: Lateral Conduction Effects on Heat-Transfer Data Obtained With the Phase-Change Paint Technique. NASA CR-2435, 1974.
24. Gillerlain, Joseph D., Jr.: Use of Phase-Change Paints To Study Fin-Body Interference Heating. NSWC/WOL/TR 75-62, U.S. Navy, Apr. 1976. (Available from DDC as AD-A027 029.)
25. Goldberg, Theodore J.; and Hefner, Jerry N. (appendix by James C. Emery): Starting Phenomena for Hypersonic Inlets With Thick Turbulent Boundary Layers at Mach 6. NASA TN D-6280, 1971.
26. Ames Research Staff: Equations, Tables, and Charts for Compressible Flow. NACA Rep. 1135, 1953. (Supersedes NACA TN 1428.)

27. Anderson, E. C.; and Lewis, C. H.: Laminar or Turbulent Boundary-Layer Flows of Perfect Gases or Reacting Gas Mixtures in Chemical Equilibrium. NASA CR-1893, 1971.
28. Harris, Julius E.: Numerical Solution of the Equations for Compressible Laminar, Transitional, and Turbulent Boundary Layers and Comparisons With Experimental Data. NASA TR R-368, 1971.
29. Hopkins, Edward J.; Keener, Earl R.; and Louie, Pearl T.: Direct Measurements of Turbulent Skin Friction on a Nonadiabatic Flat Plate at Mach Number 6.5 and Comparisons With Eight Theories. NASA TN D-5675, 1970.
30. Johnson, Charles B.; and Boney, Lillian R.: A Simple Integral Method for the Calculation of Real-Gas Turbulent Boundary Layers With Variable Edge Entropy. NASA TN D-6217, 1971.
31. Sterrett, James R.; and Emery, James C.: Extension of Boundary-Layer-Separation Criteria to a Mach Number of 6.5 by Utilizing Flat Plates With Forward-Facing Steps. NASA TN D-618, 1960.



Hypersonic research airplane



Wing-elevon model

Figure 1.- Outlines of typical hypersonic research airplane and of wing-elevon model.

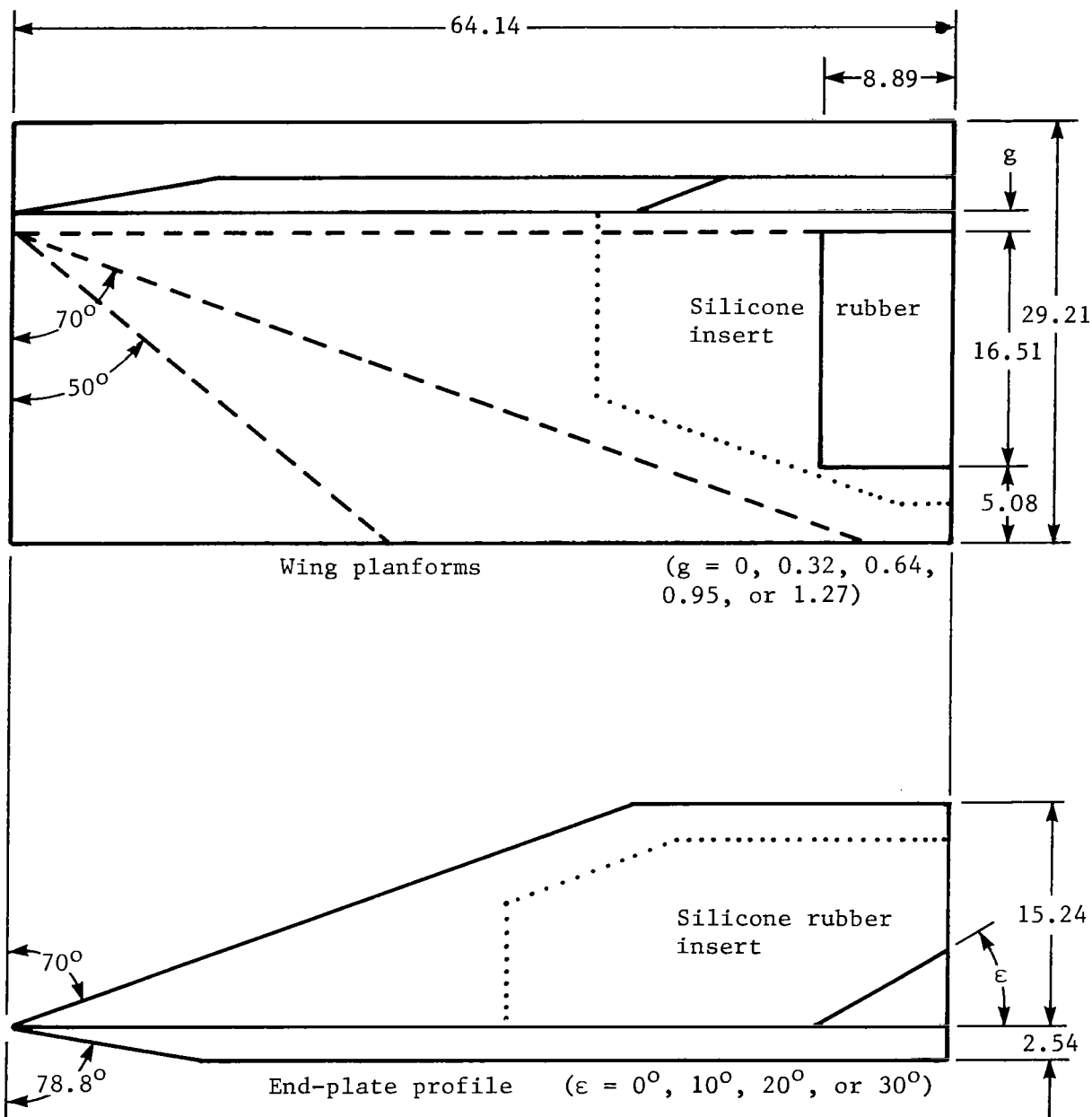


Figure 2.- Wing and end-plate planforms for wing-elevon model. Linear dimensions are in cm.



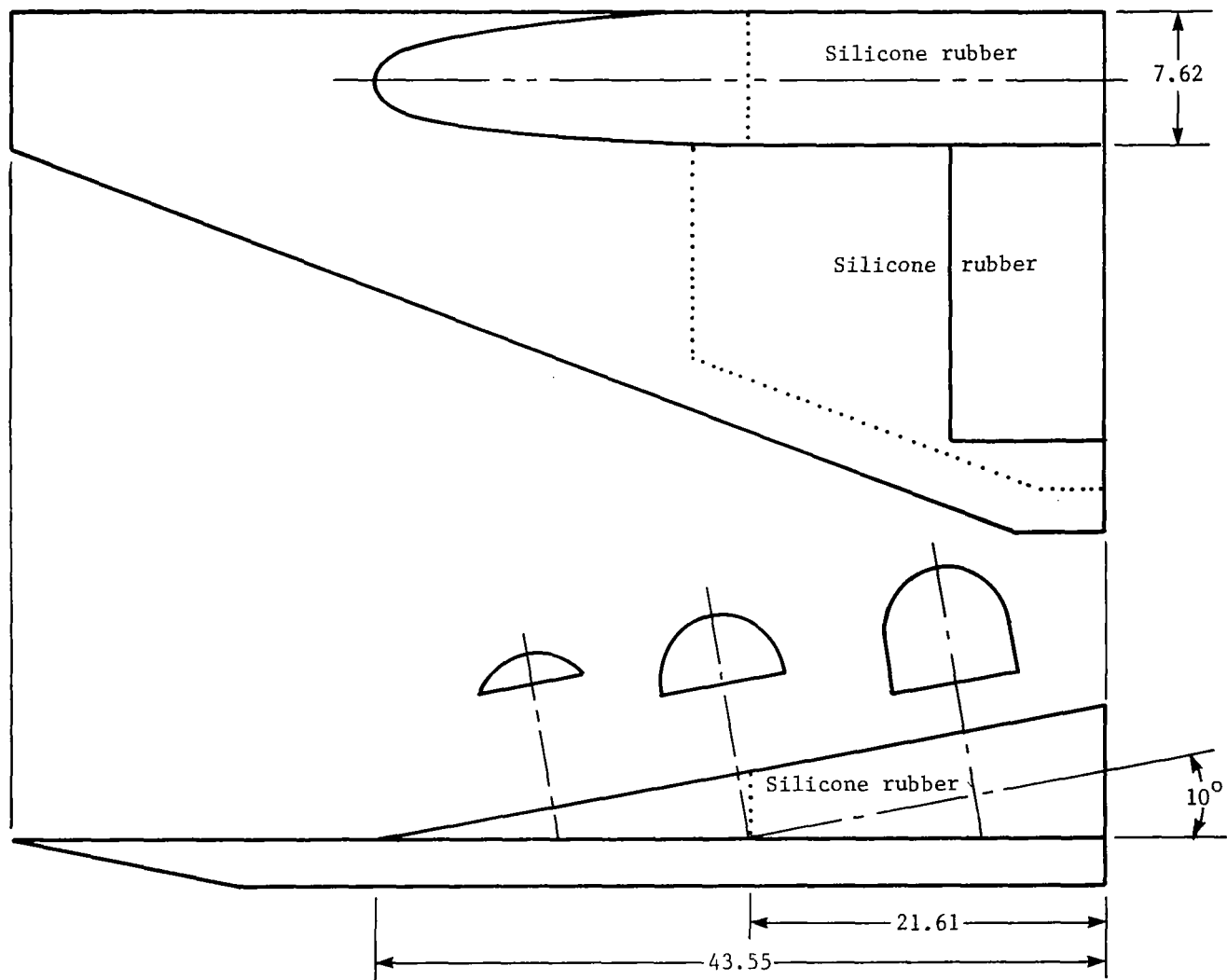


Figure 3.- Cylindrical body attached to 70° wing. Linear dimensions are in cm.

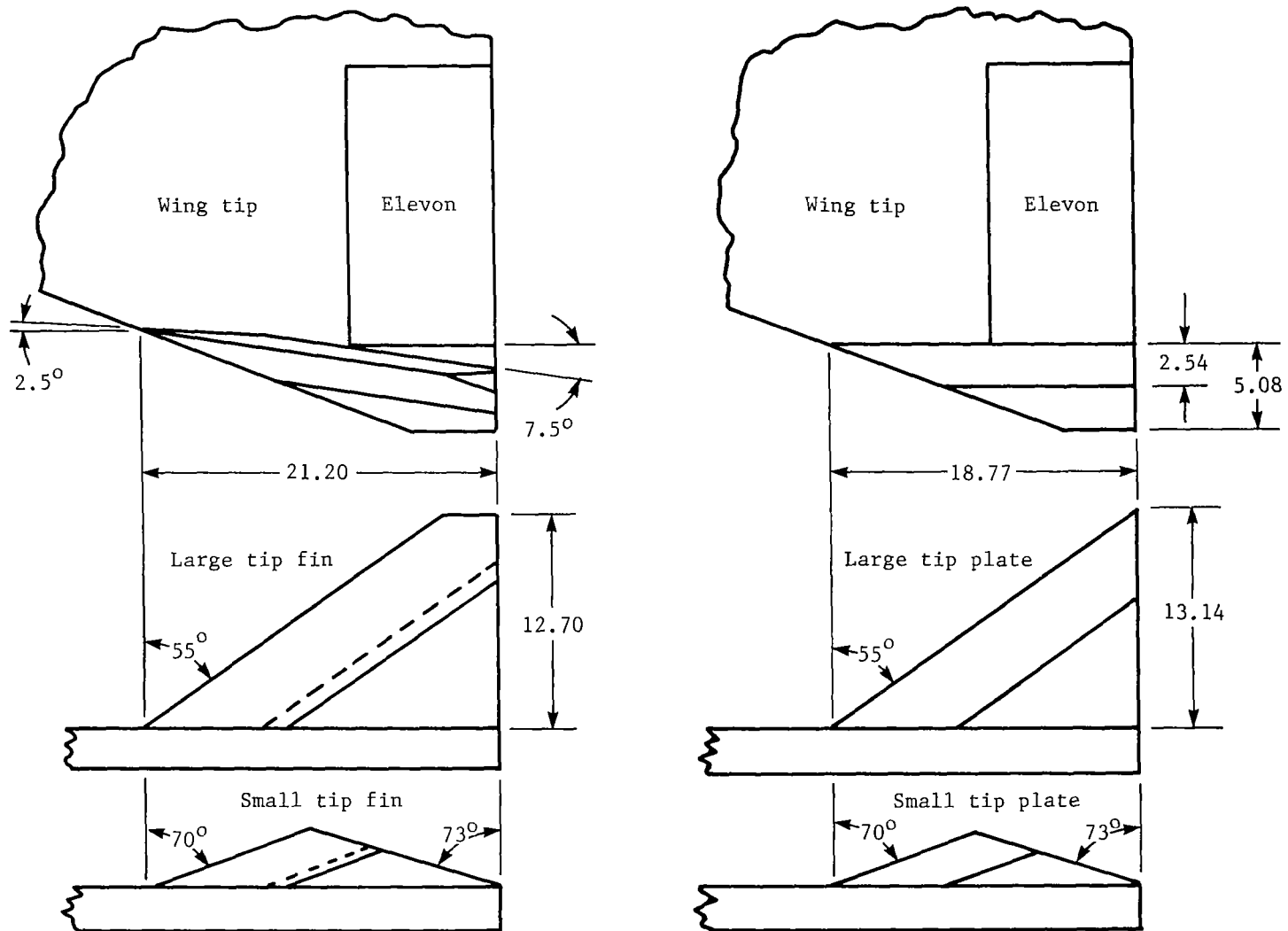
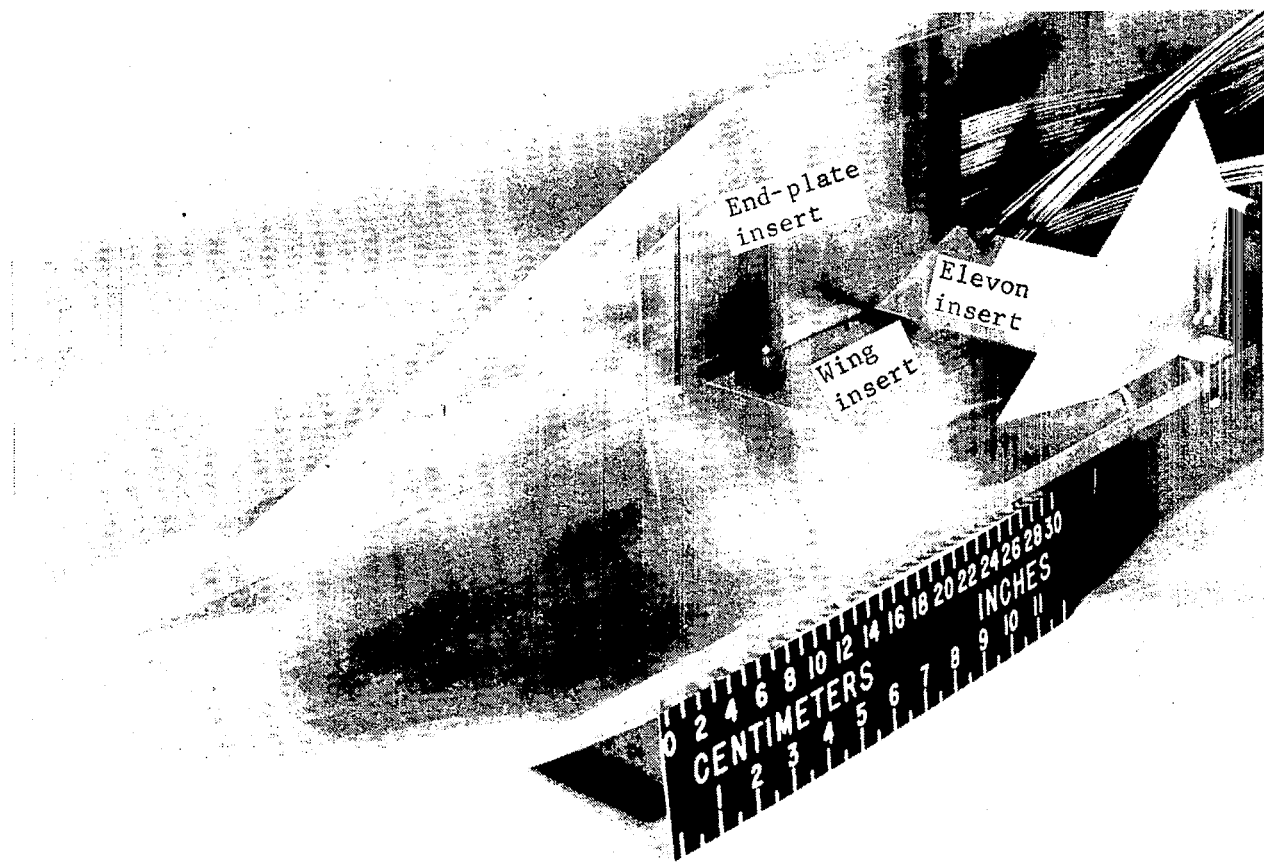
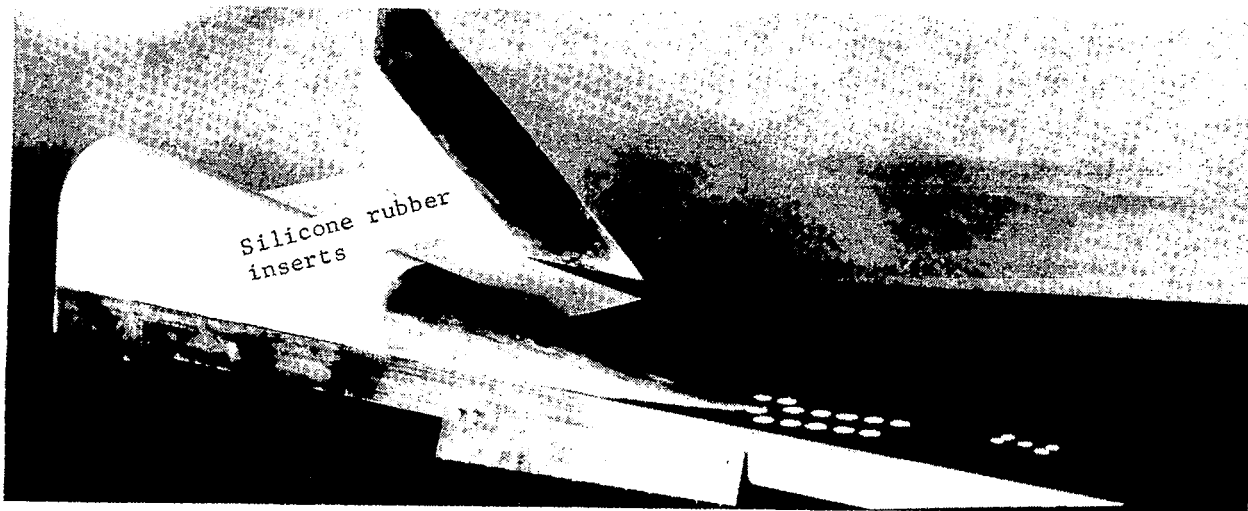


Figure 4.- Attachable tip fins and plates. Linear dimensions are in cm.

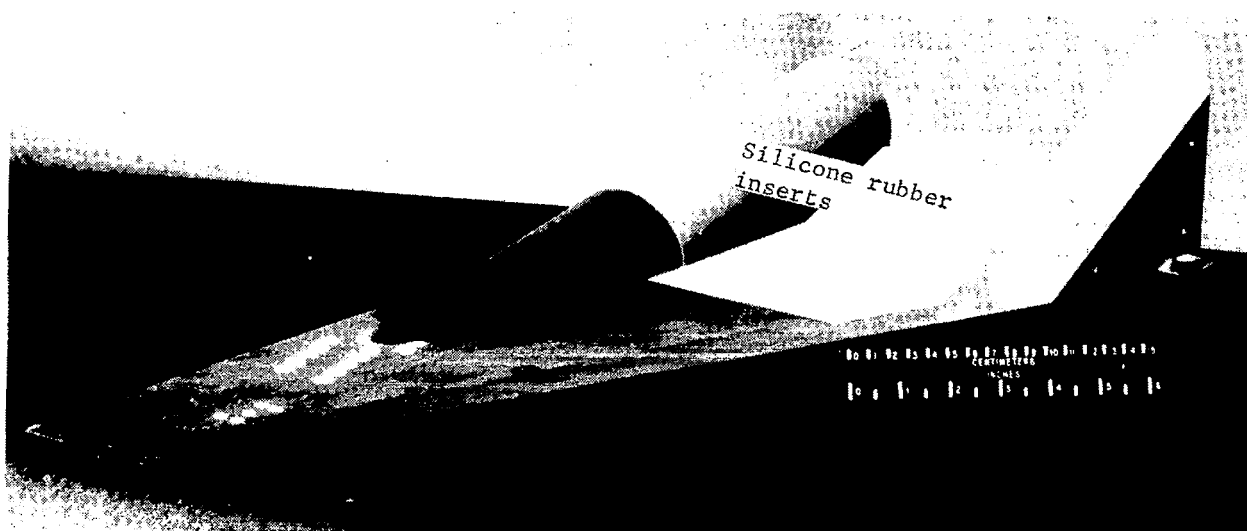


L-74-3122.1

Figure 5.- Configuration of unswept-wing—elevon model with large tip plate, 30° elevon, end plate, and pressure inserts.



L-76-5852.1



L-76-5853.1

Figure 6.- Configuration of wing-elevon model;  $70^\circ$  wing with cylindrical body, large tip fin, and  $20^\circ$  elevon.

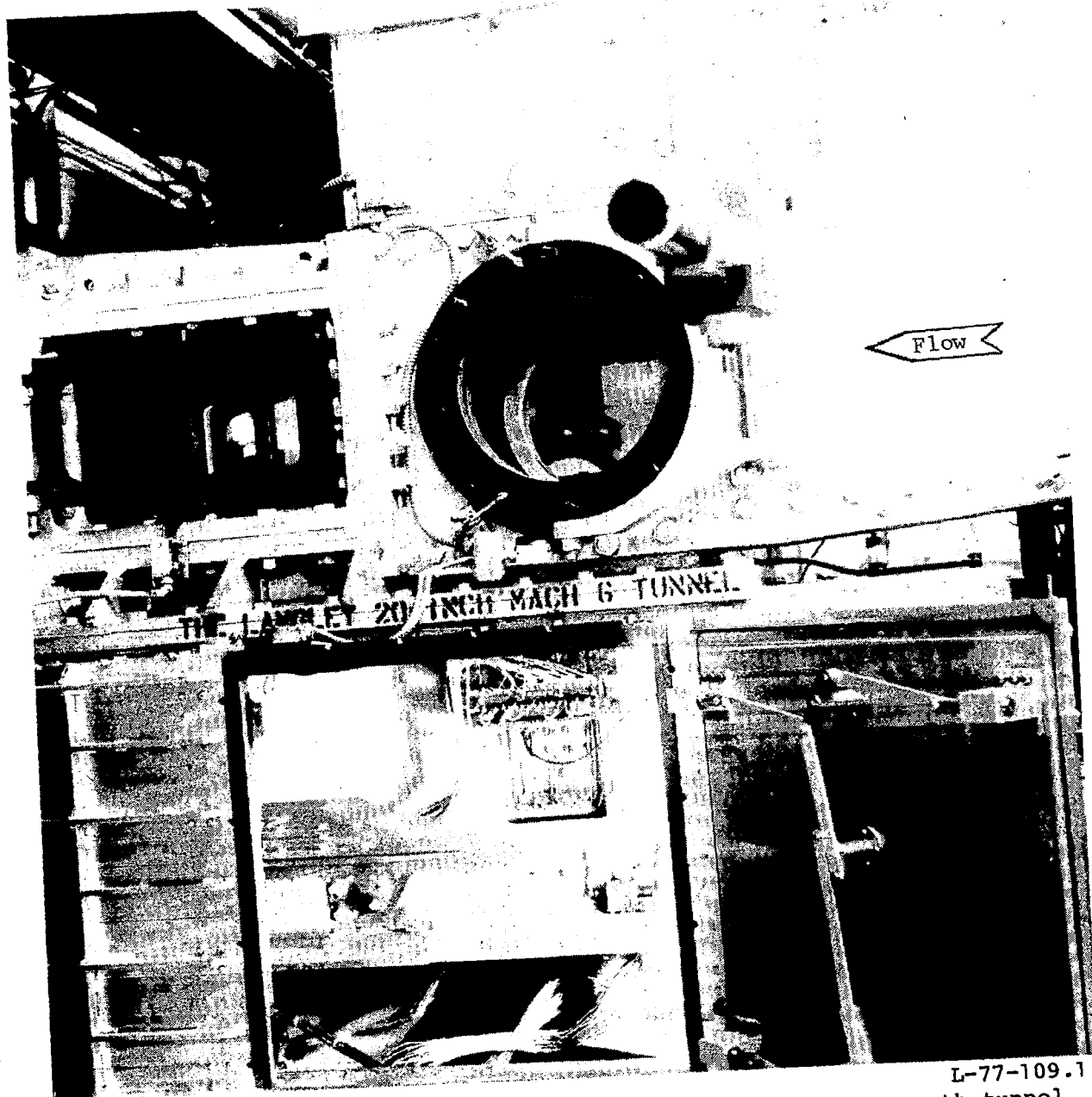
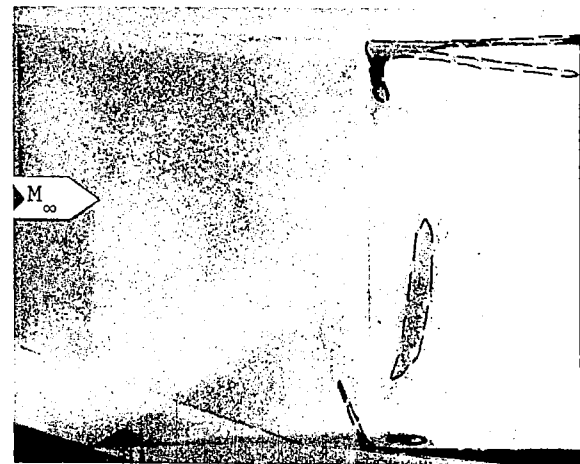


Figure 7.- Model mounted on injection system in chamber beneath tunnel test section.



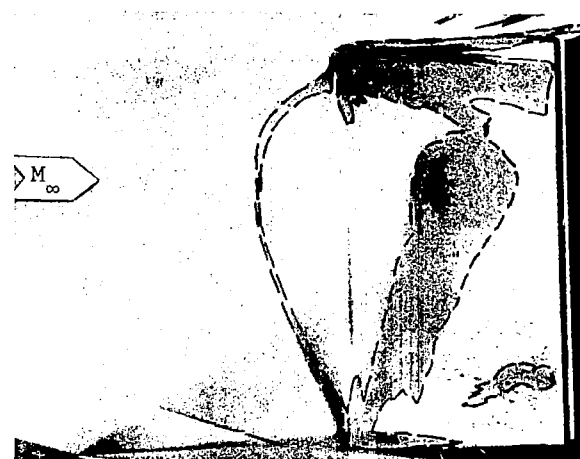
Frame 4



Frame 18



Frame 50



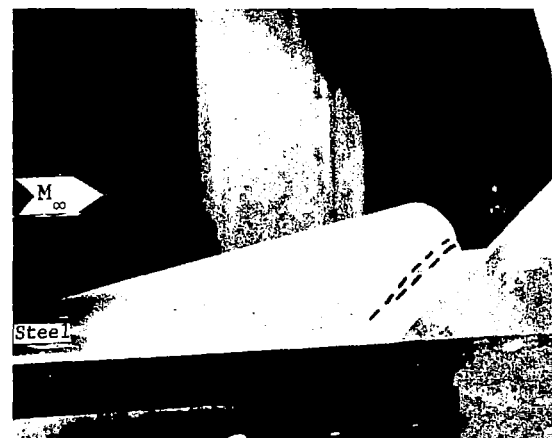
Frame 118

L-78-50

Figure 8.- Sample frames from planform motion pictures of phase-change paint showing progression of melted paint regions, with time, for the 70° wing with cylindrical body, large tip fin, and 30° elevon.



Frame 4



Frame 18



Frame 50



Frame 118

L-78-51

Figure 9.- Sample frames from profile motion pictures of phase-change paint showing progression of melted paint regions, with time, for the 70° wing with cylindrical body, large tip fin, and 30° elevon.

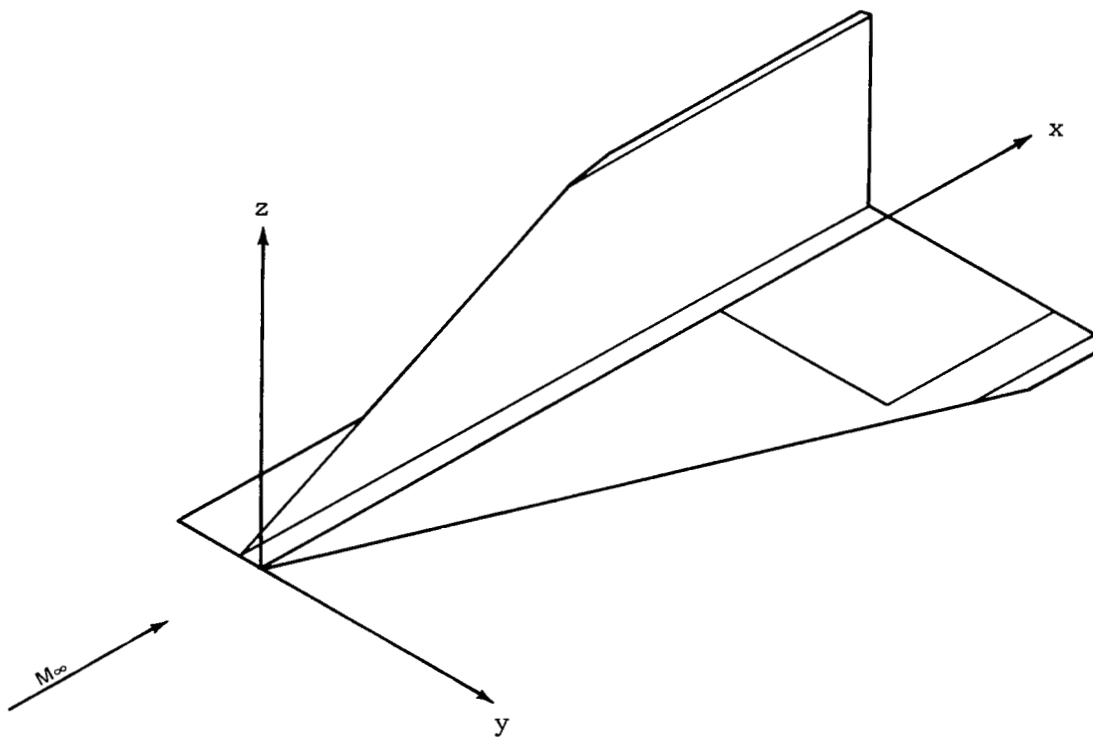
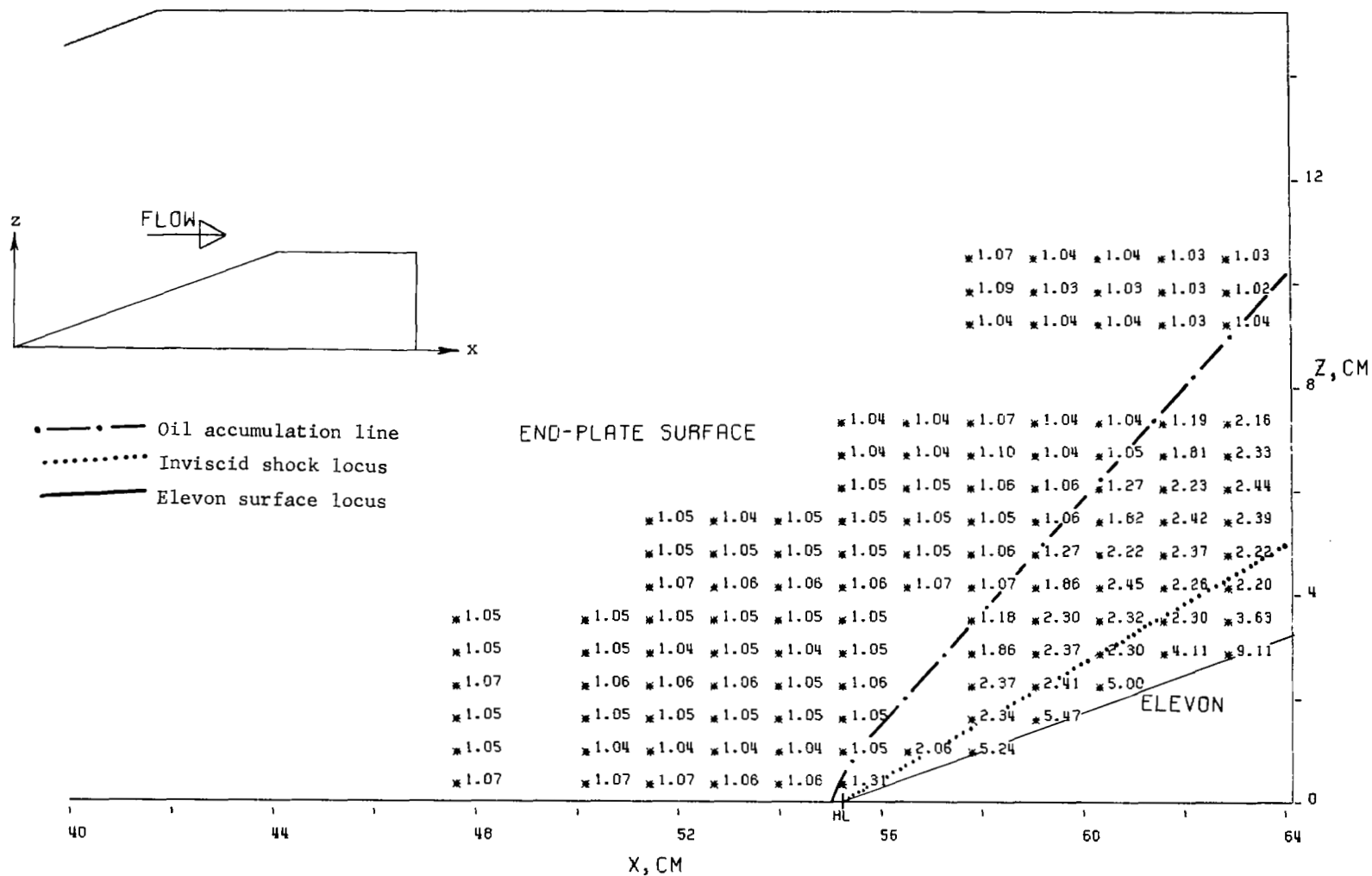
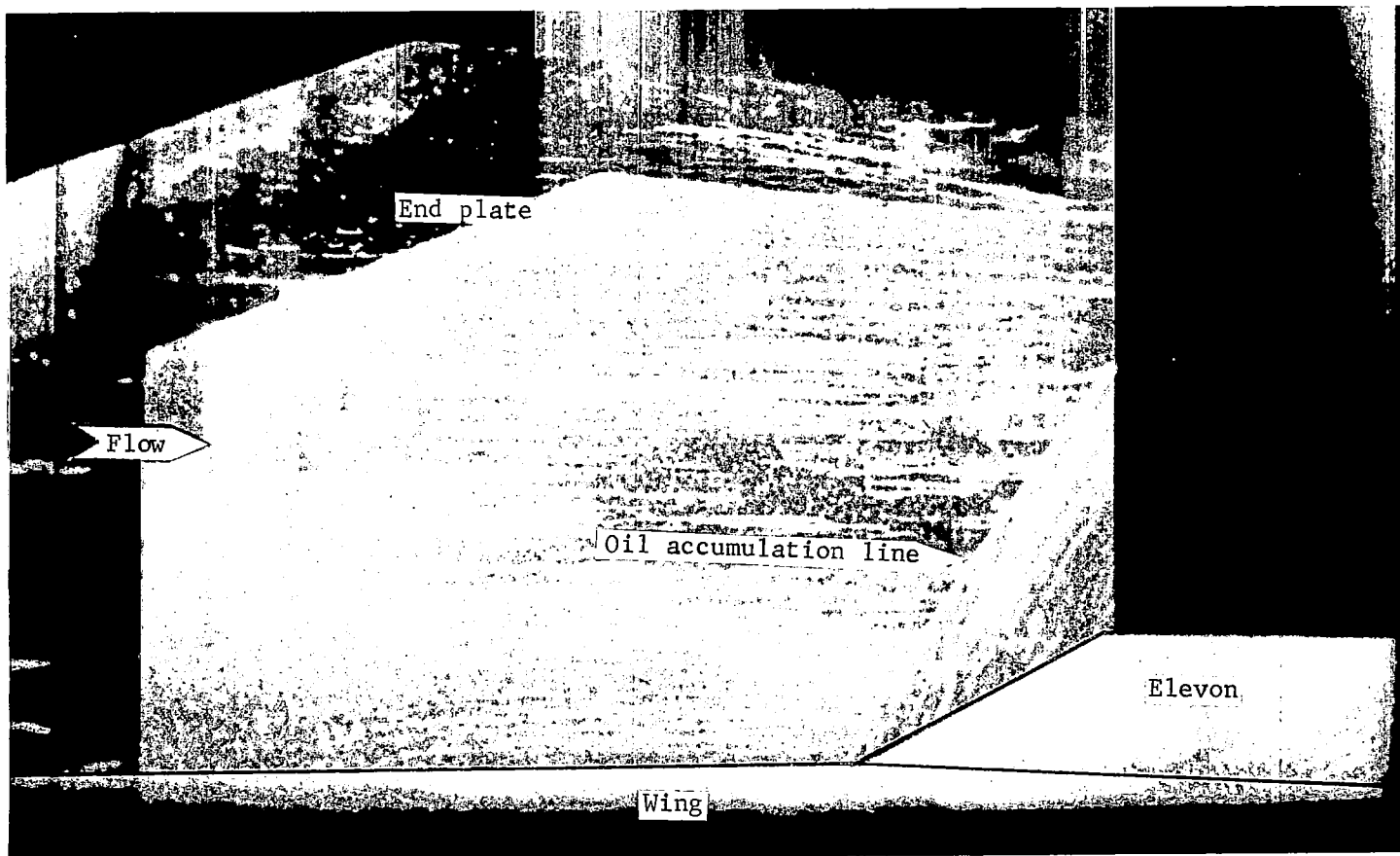


Figure 10.- Coordinate system.









L-78-167

Figure 13.- Frame from profile oil-flow motion picture showing oil accumulation line on end-plate surface for a  $20^\circ$  elevon deflection ( $\Lambda = 0$ ).

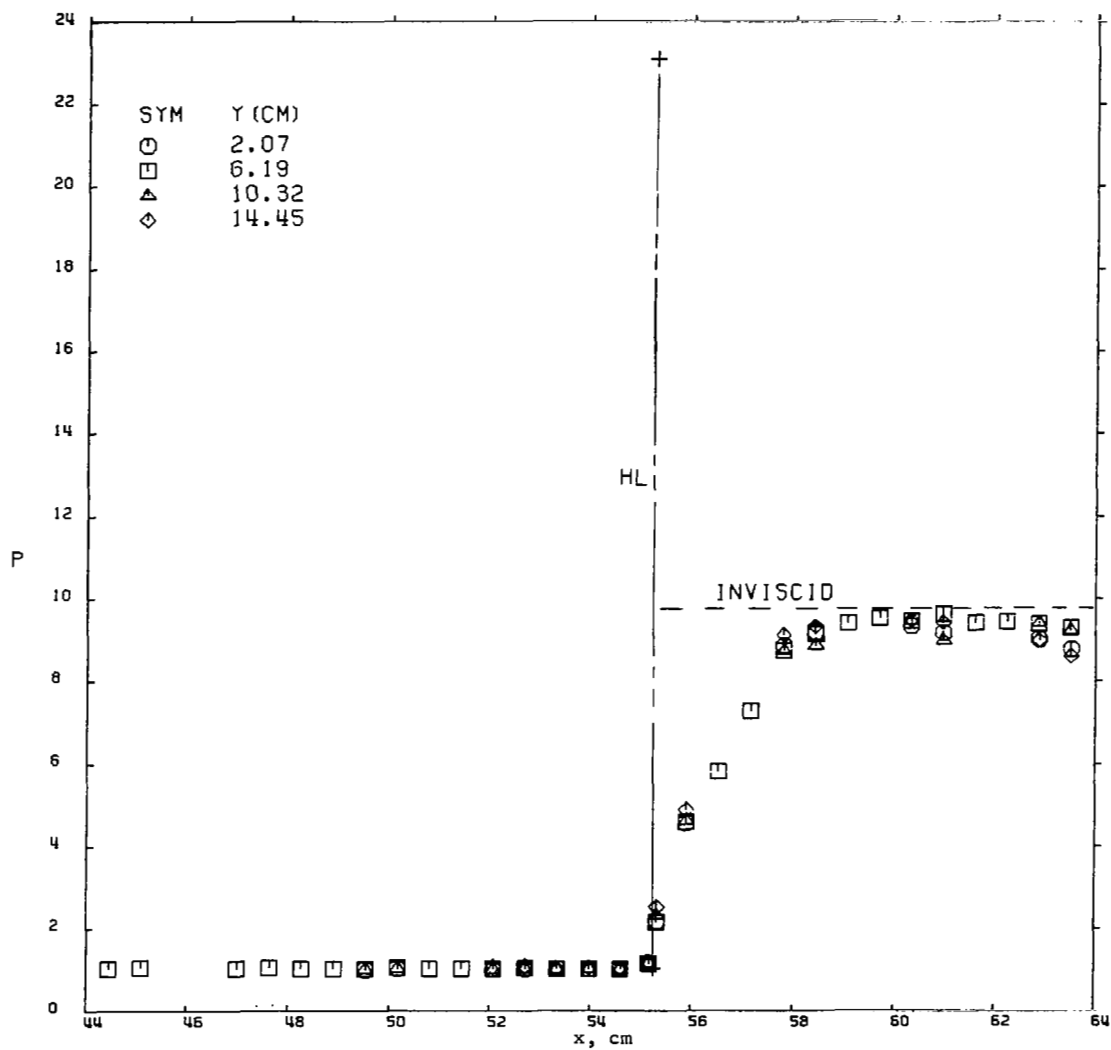


Figure 14.- Streamwise pressure-ratio distributions on wing and elevon surfaces for  $\epsilon = 20^\circ$  and  $\Lambda = 0^\circ$ .

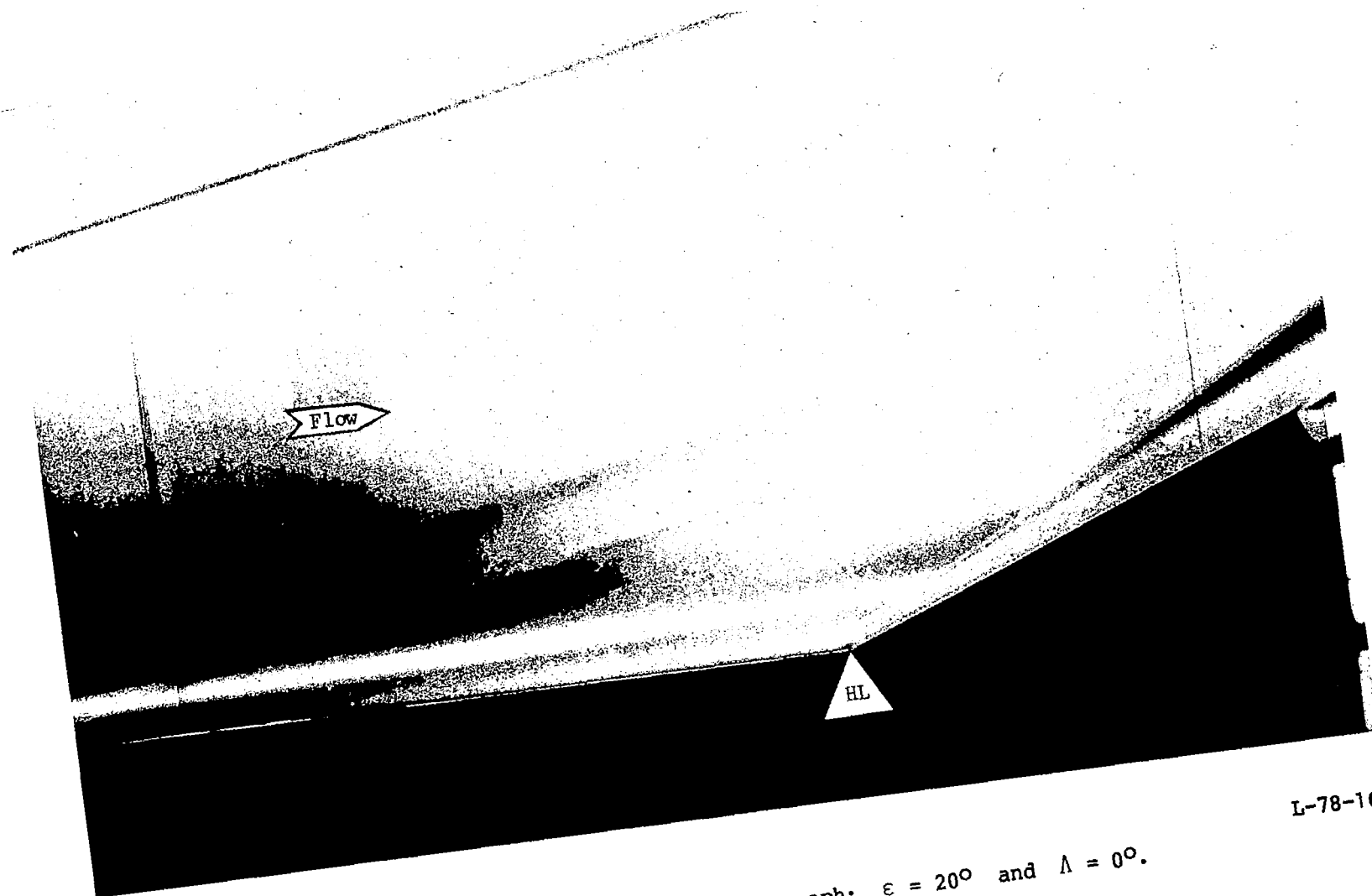


Figure 15.- Schlieren flow photograph;  $\epsilon = 20^\circ$  and  $\Lambda = 0^\circ$ .

L-78-168

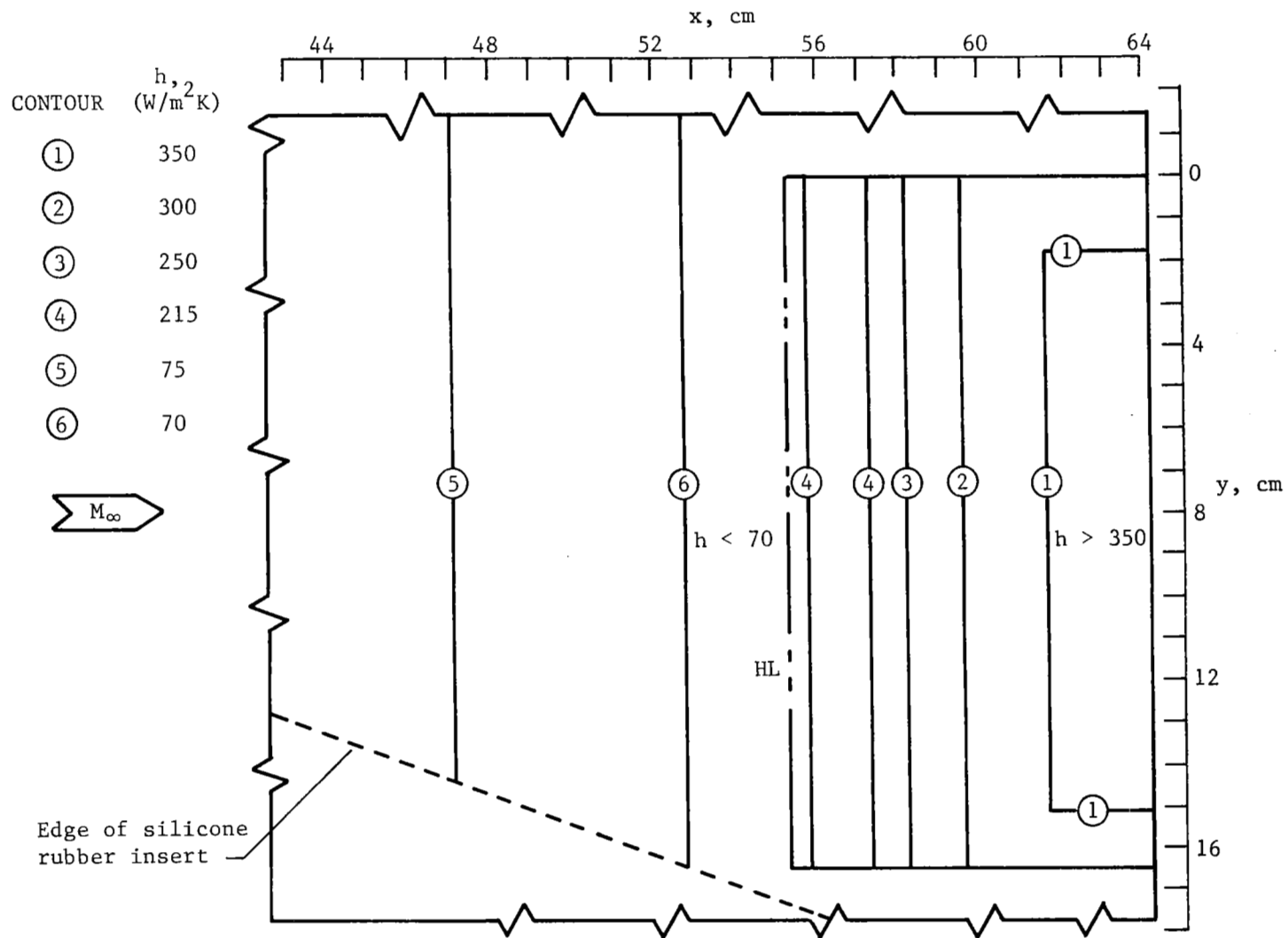


Figure 16.- Contours of constant heat-transfer-rate coefficient  $h$  on wing and elevon surfaces;  $\epsilon = 20^\circ$  and  $\Lambda = 0^\circ$ .

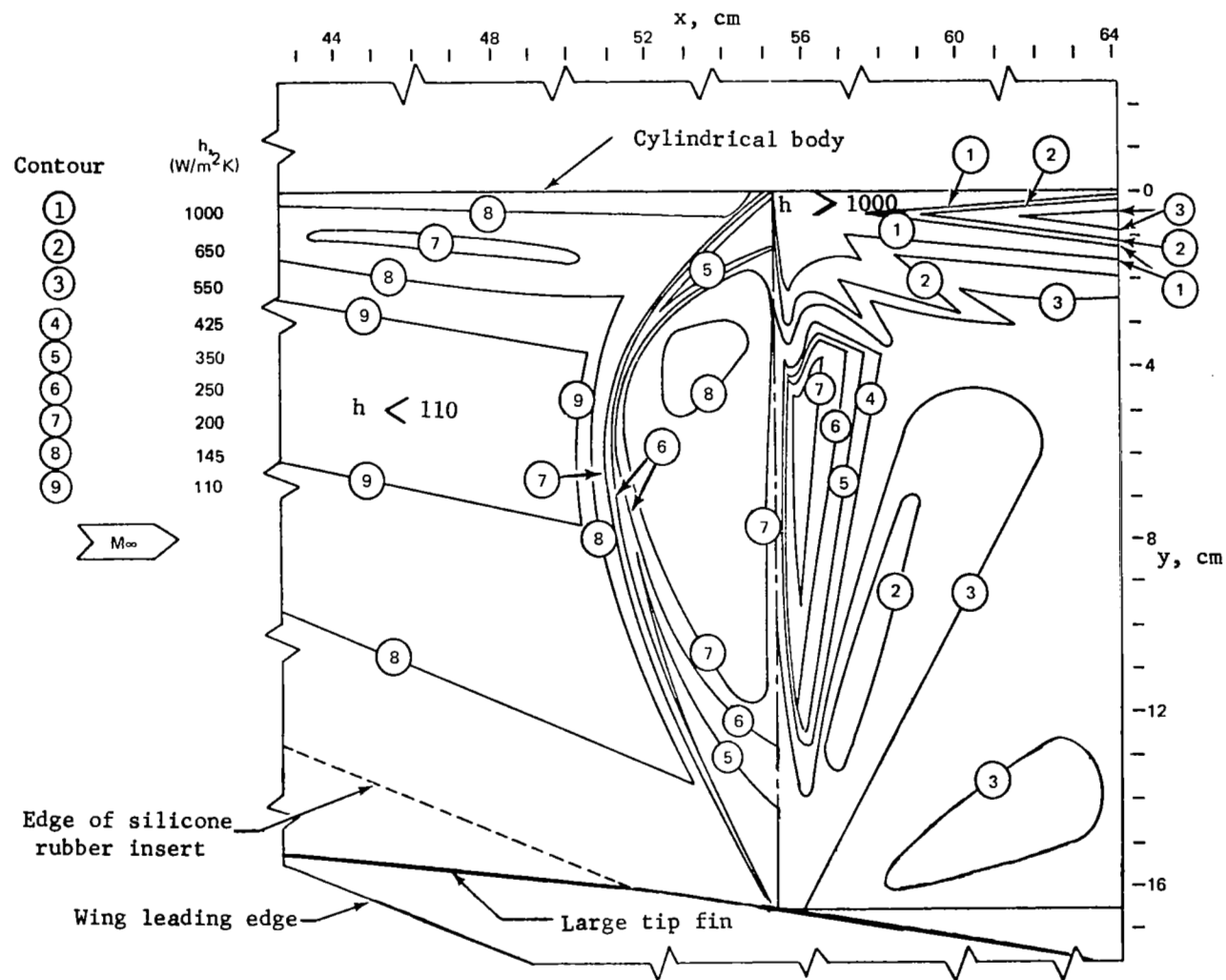


Figure 17.- Contours of constant heat-transfer-rate coefficient  $h$  on wing and elevon surfaces;  $\epsilon = 30^\circ$ ,  $\Lambda = 70^\circ$ , cylindrical body and large tip fin attached.

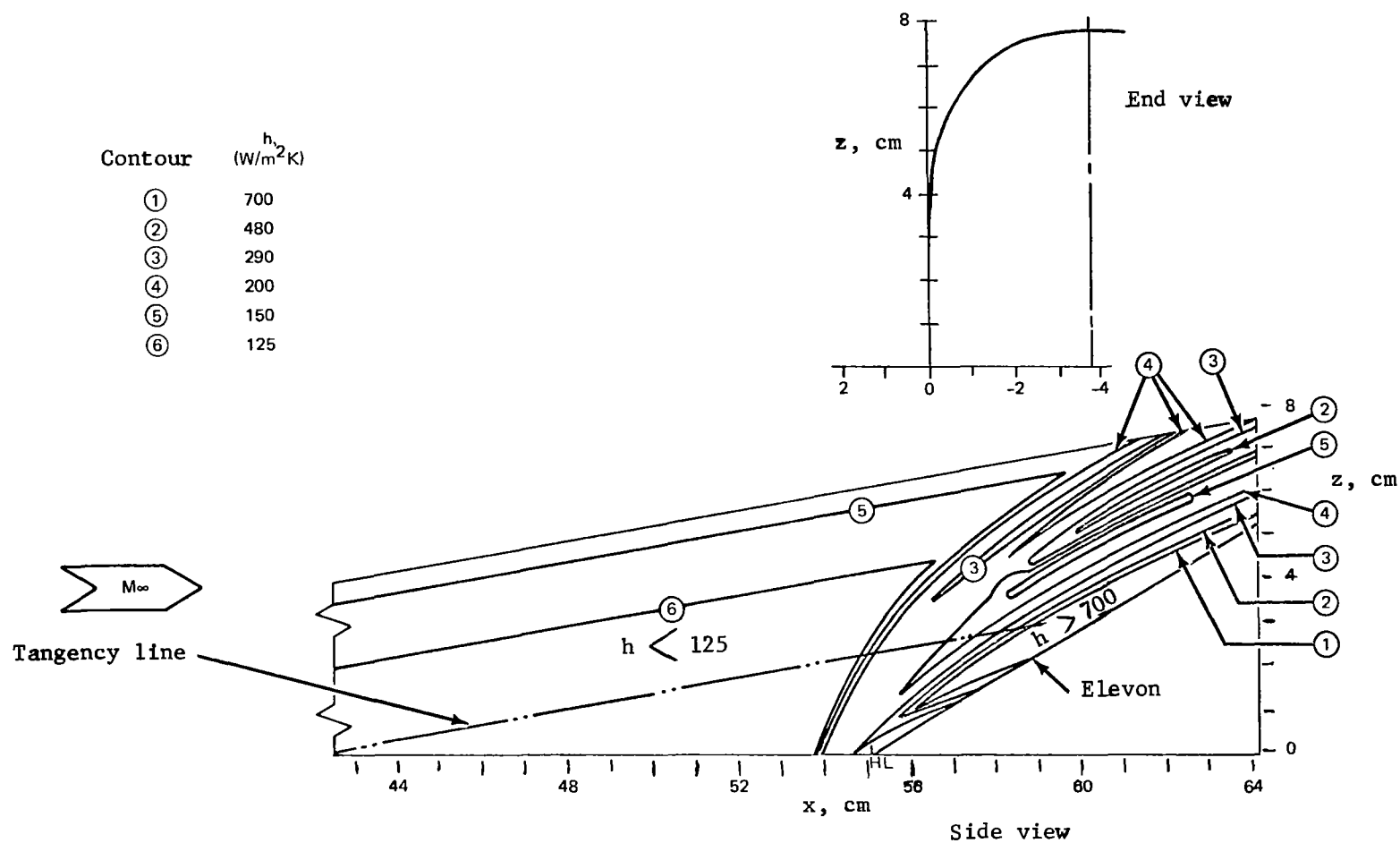
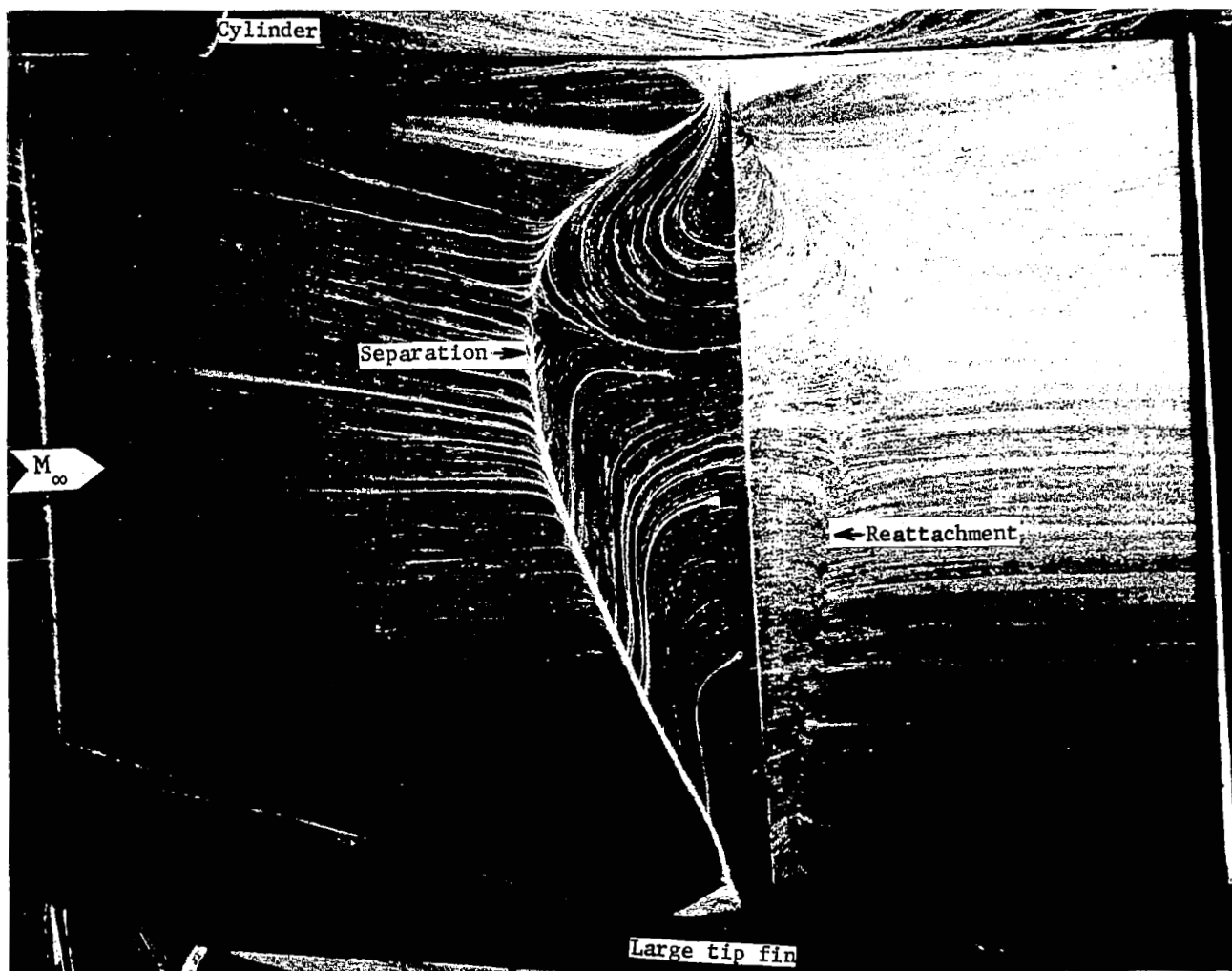


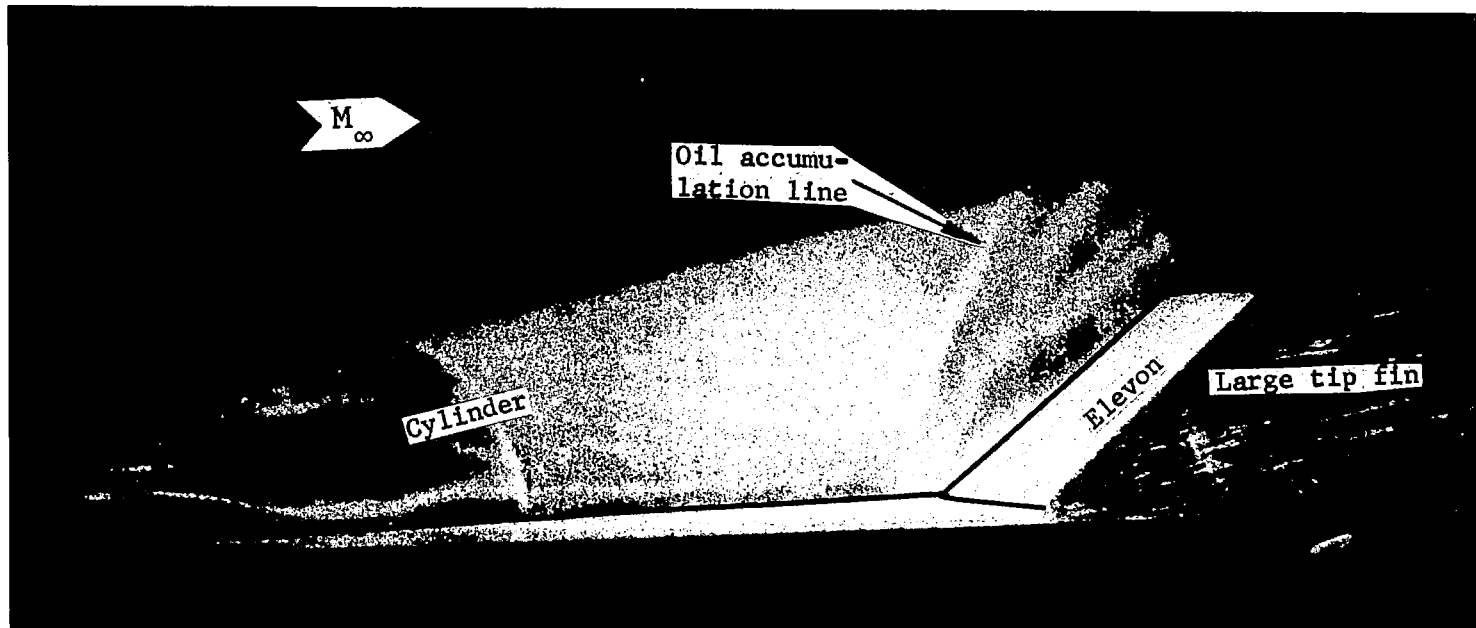
Figure 18.- Contours of constant heat-transfer-rate coefficient  $h$  on cylindrical-body surface;  $\epsilon = 30^\circ$ ,  $\Lambda = 70^\circ$ , large tip fin attached.





L-78-70

Figure 19.- Frame from planform oil-flow motion picture showing wing and elevon surfaces;  $\epsilon = 30^\circ$ ,  $\Lambda = 70^\circ$ , cylindrical body and large tip fin attached.



L-78-77

Figure 20.- Frame from profile oil-flow motion picture showing cylindrical body surface;  
 $\epsilon = 30^\circ$ ,  $\Lambda = 70^\circ$ , large tip fin attached.

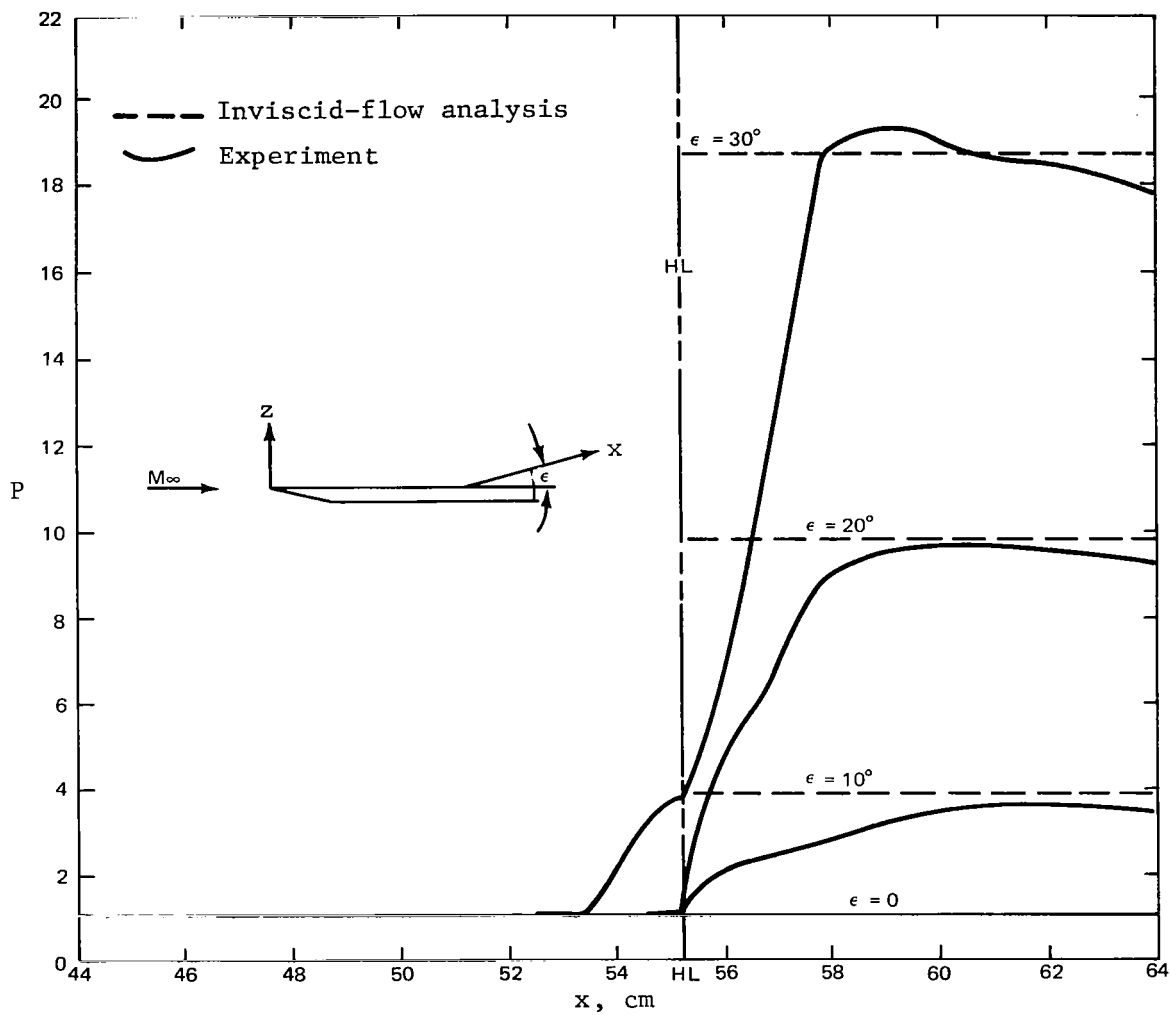


Figure 21.- Streamwise pressure-ratio distributions along elevon midspan line ( $y = 8.26$  cm) on unswept-wing and elevon surfaces.

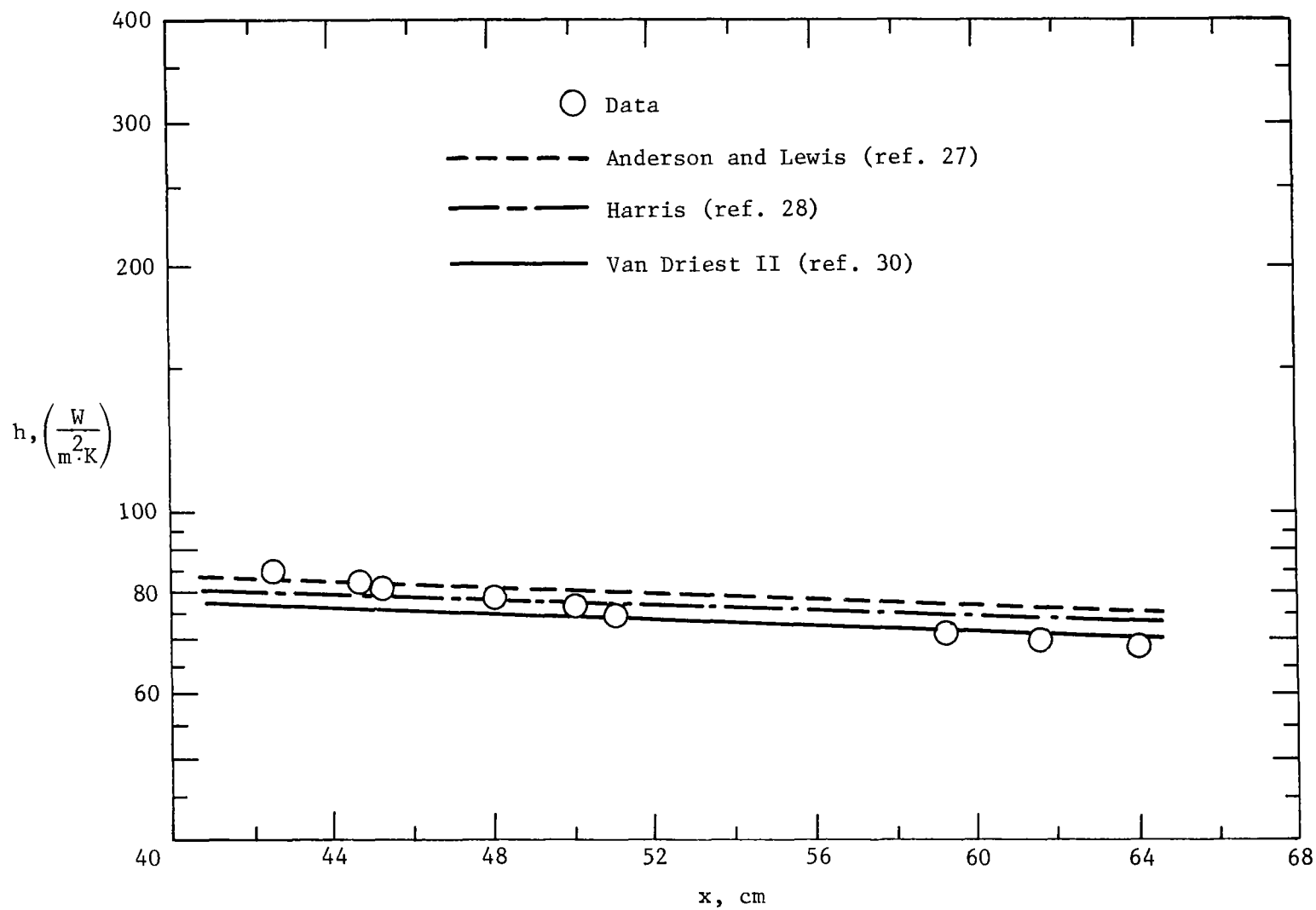


Figure 22.- Streamwise distributions along elevon midspan line, of heat-transfer-rate coefficients on unswept-wing and undeflected-elevon surfaces.

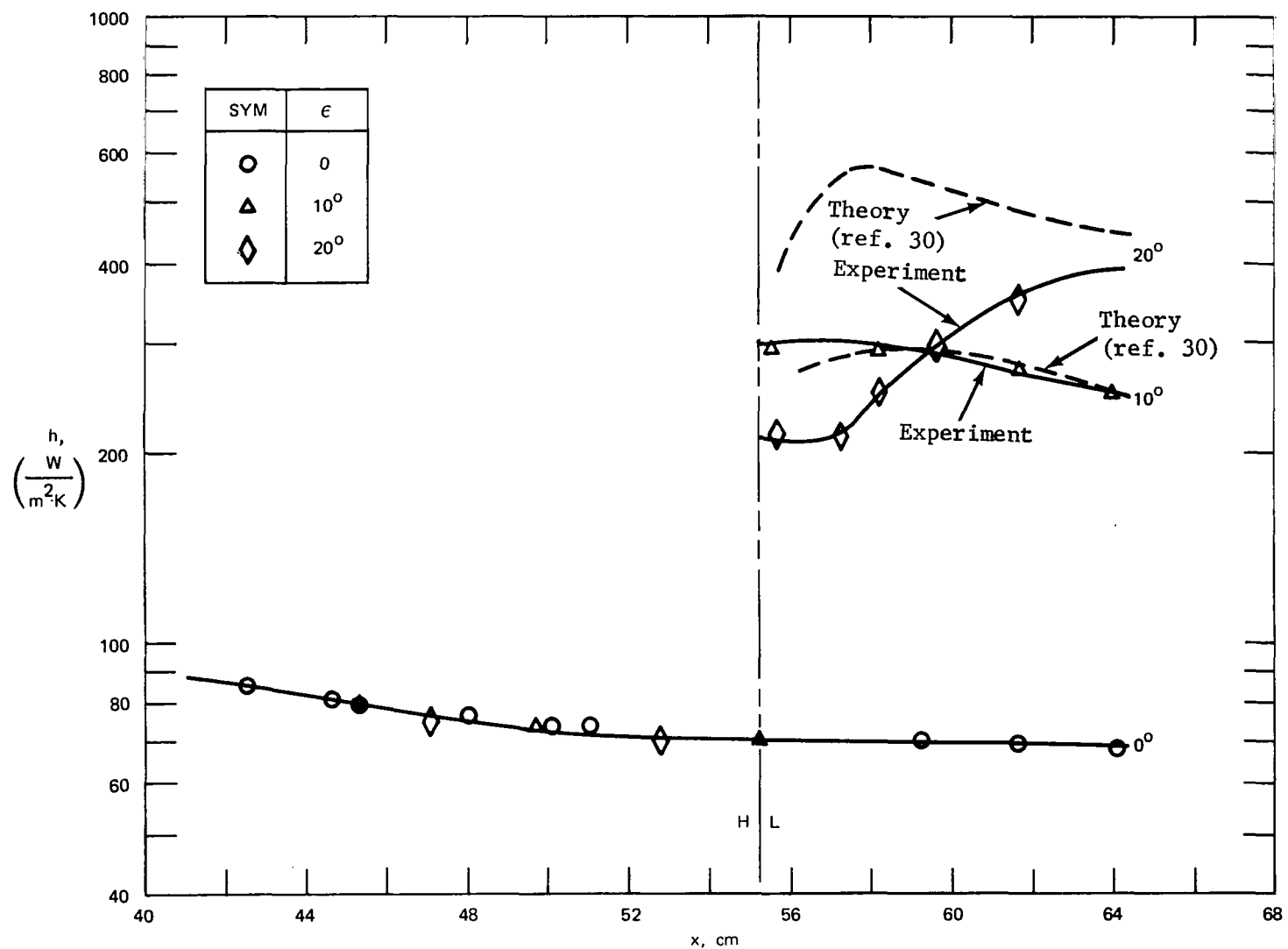


Figure 23.- Streamwise distributions of heat-transfer-rate coefficients on unswept-wing and 0°-, 10°-, and 20°-elevon surfaces along elevon midspan line.

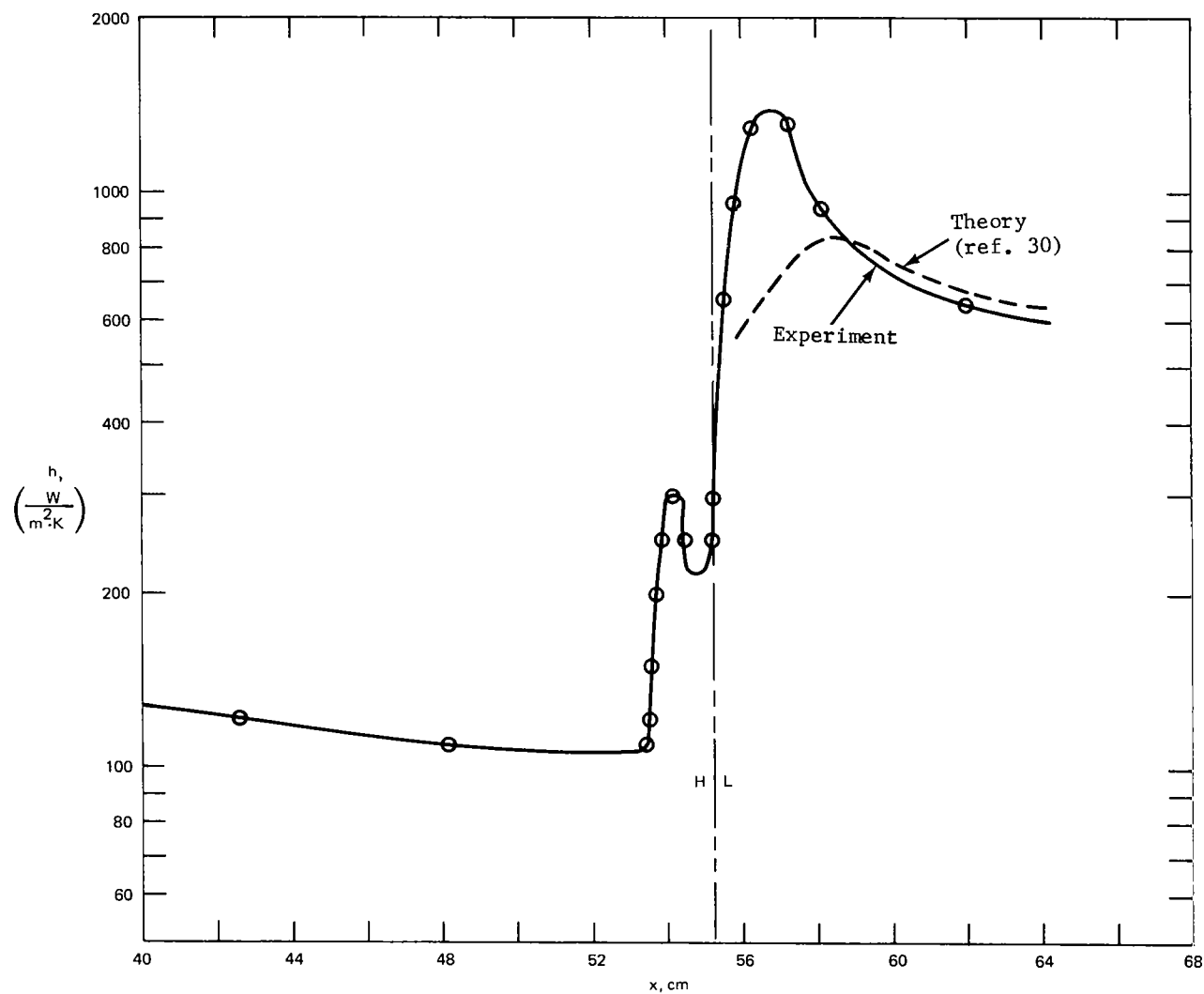


Figure 24.- Streamwise distribution of heat-transfer-rate coefficients on unswept-wing and 30°-elevon surfaces along elevon midspan line.

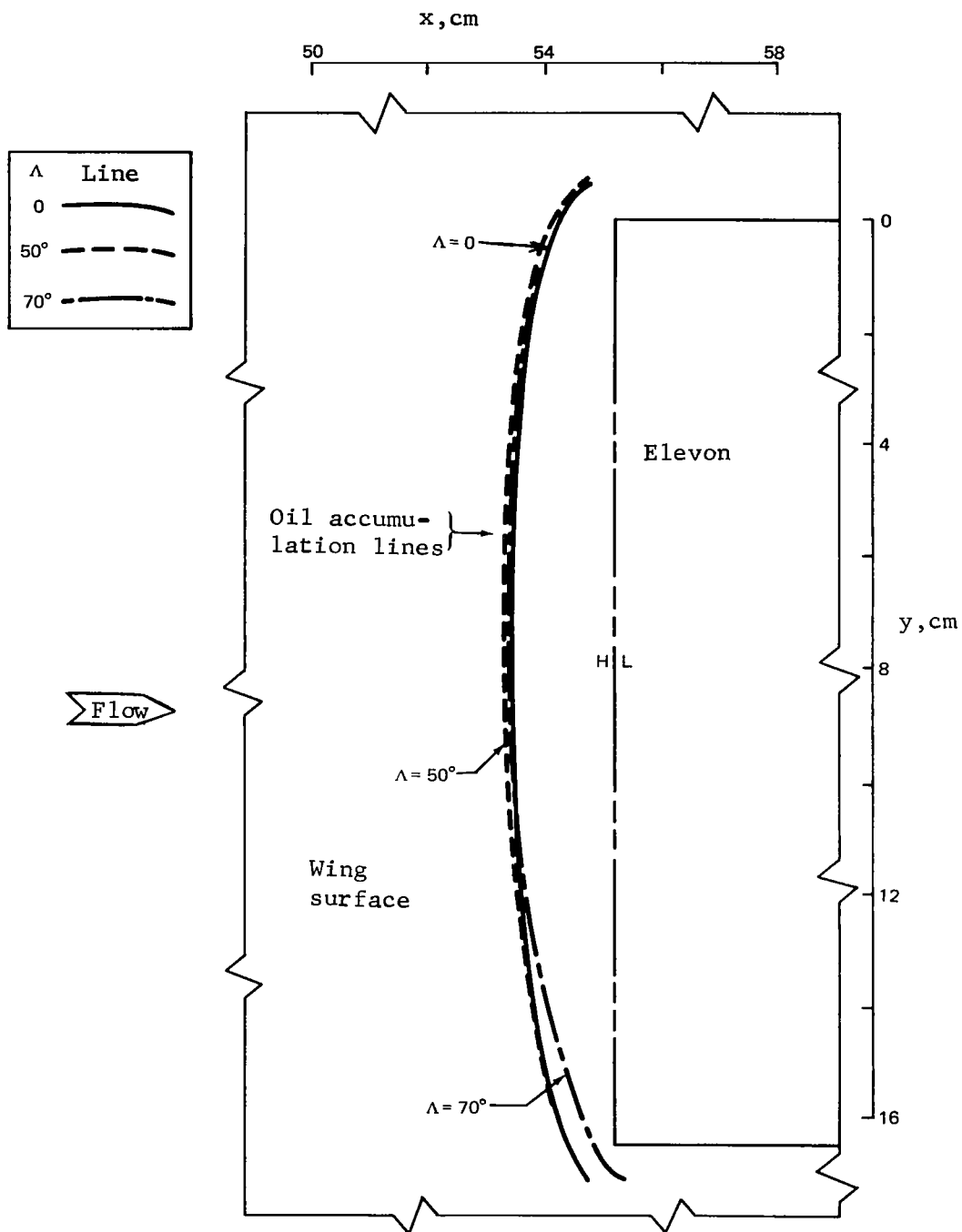
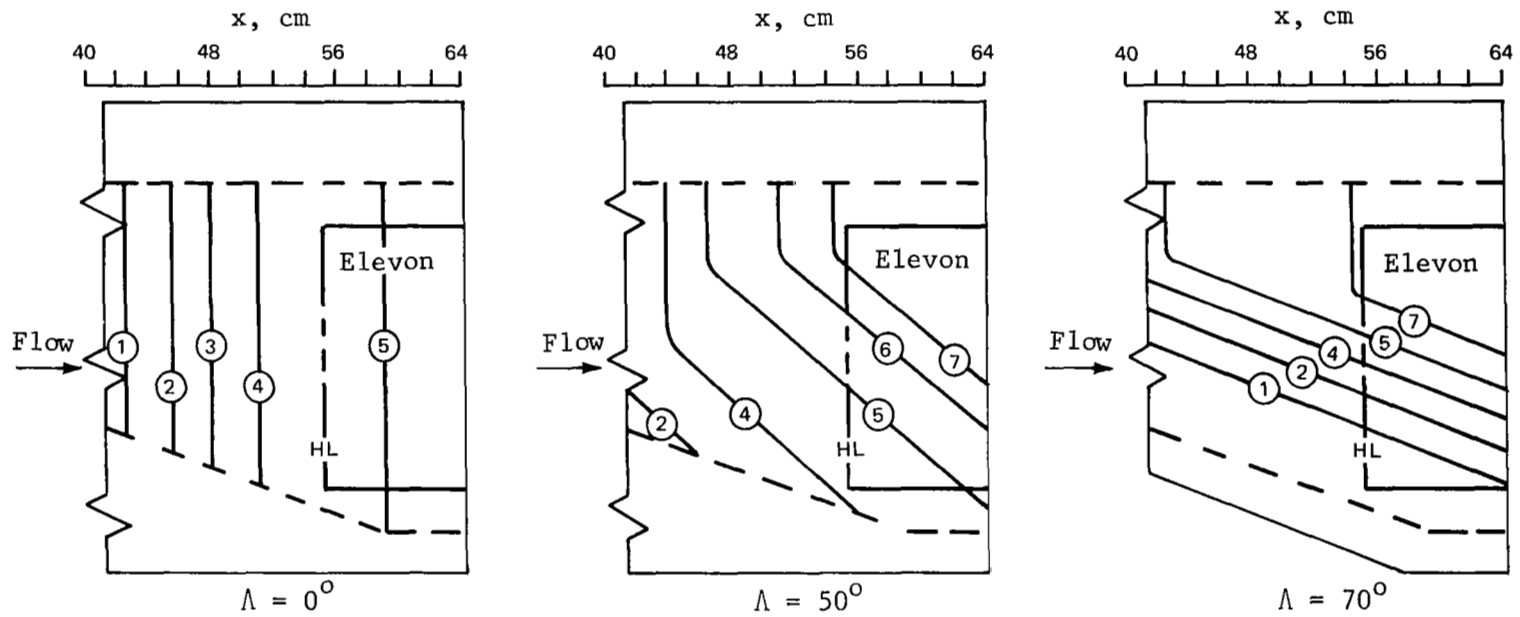


Figure 25.- Wing-sweep effects on oil accumulation lines upstream of 30° elevon.



Dashed lines (---) indicate boundaries of silicone rubber inserts

Contour no.:	①	②	③	④	⑤	⑥	⑦
$h_2$ (W/m <sup>2</sup> .K)	85	80	78	75	70	68	65

Figure 26.- Wing sweepback effects on contours of constant heat-transfer-rate coefficients on wing and undeflected-elevon surfaces.



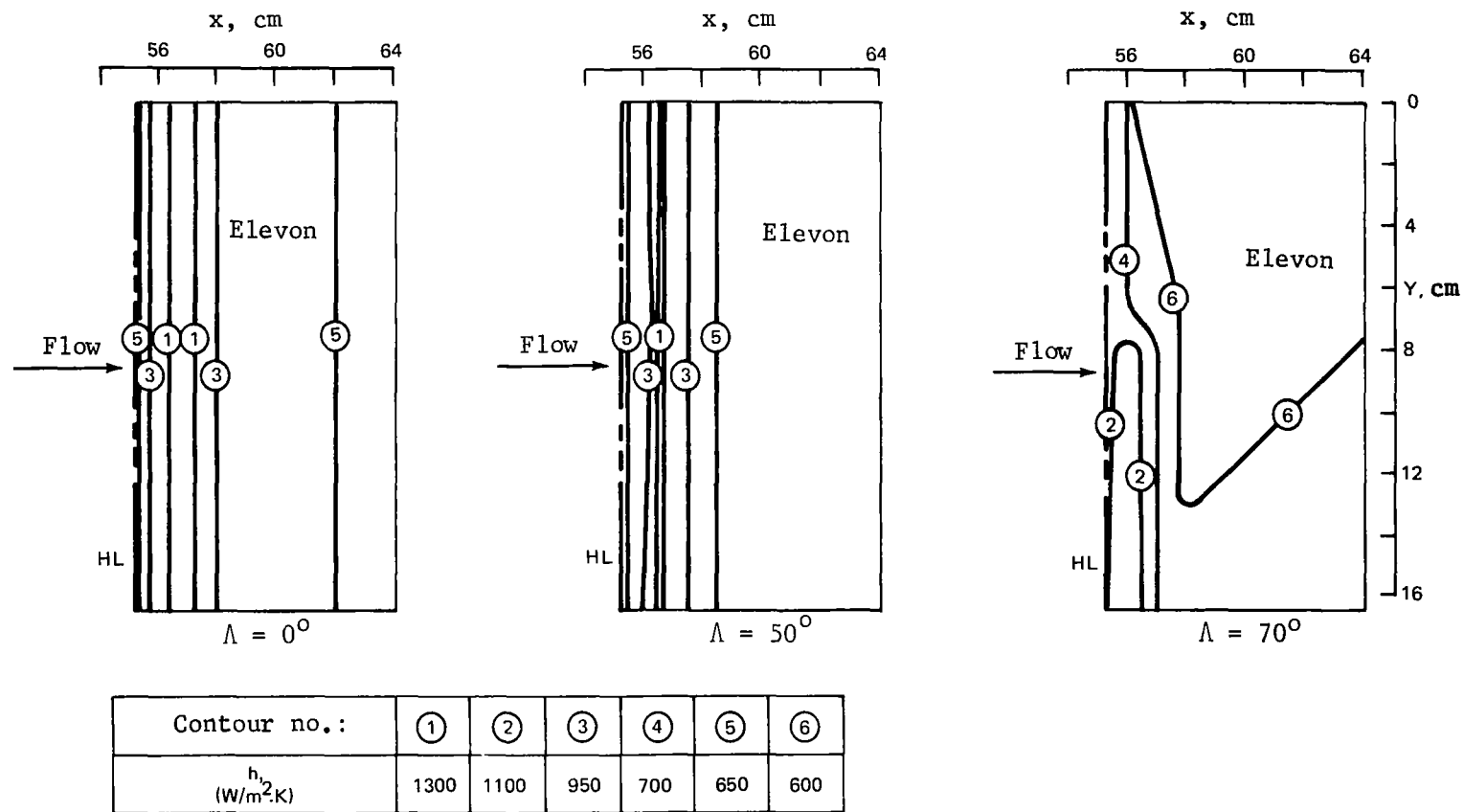


Figure 27.- Wing sweepback effects on contours of constant heat-transfer-rate coefficients on 30°-elevon surface.

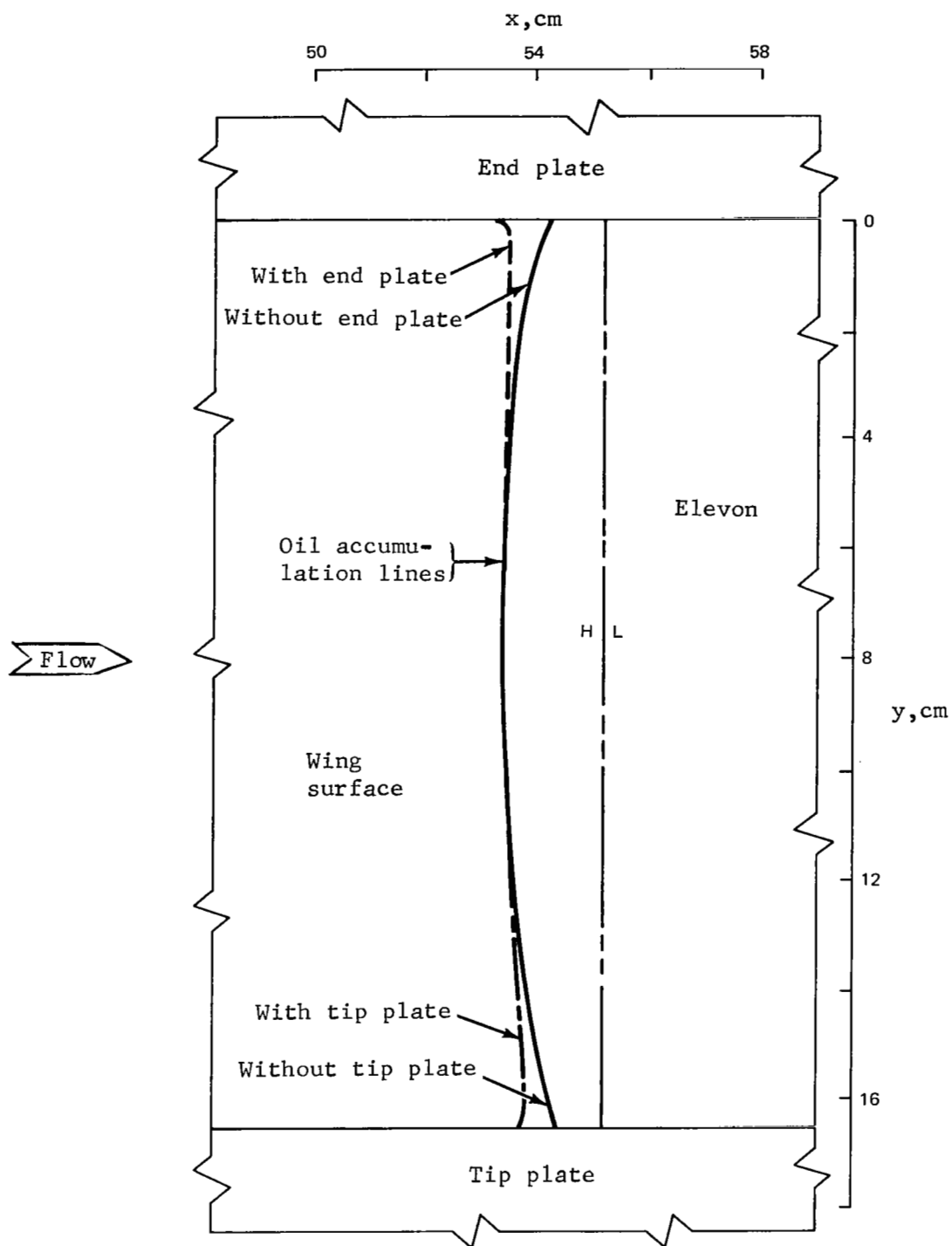


Figure 28.- End-plate and tip-plate effects on oil accumulation lines upstream of  $30^\circ$  elevon on unswept wing.

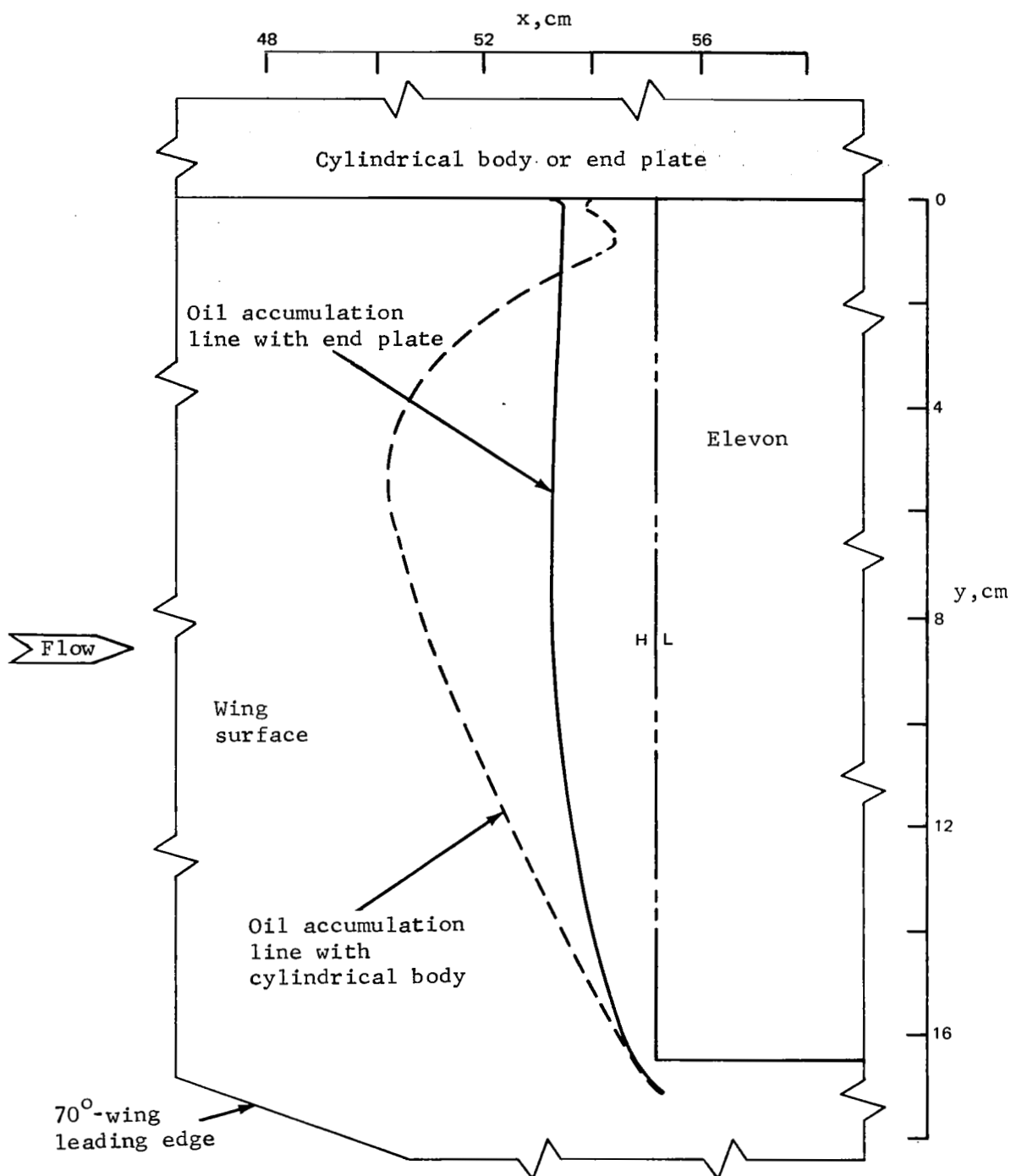
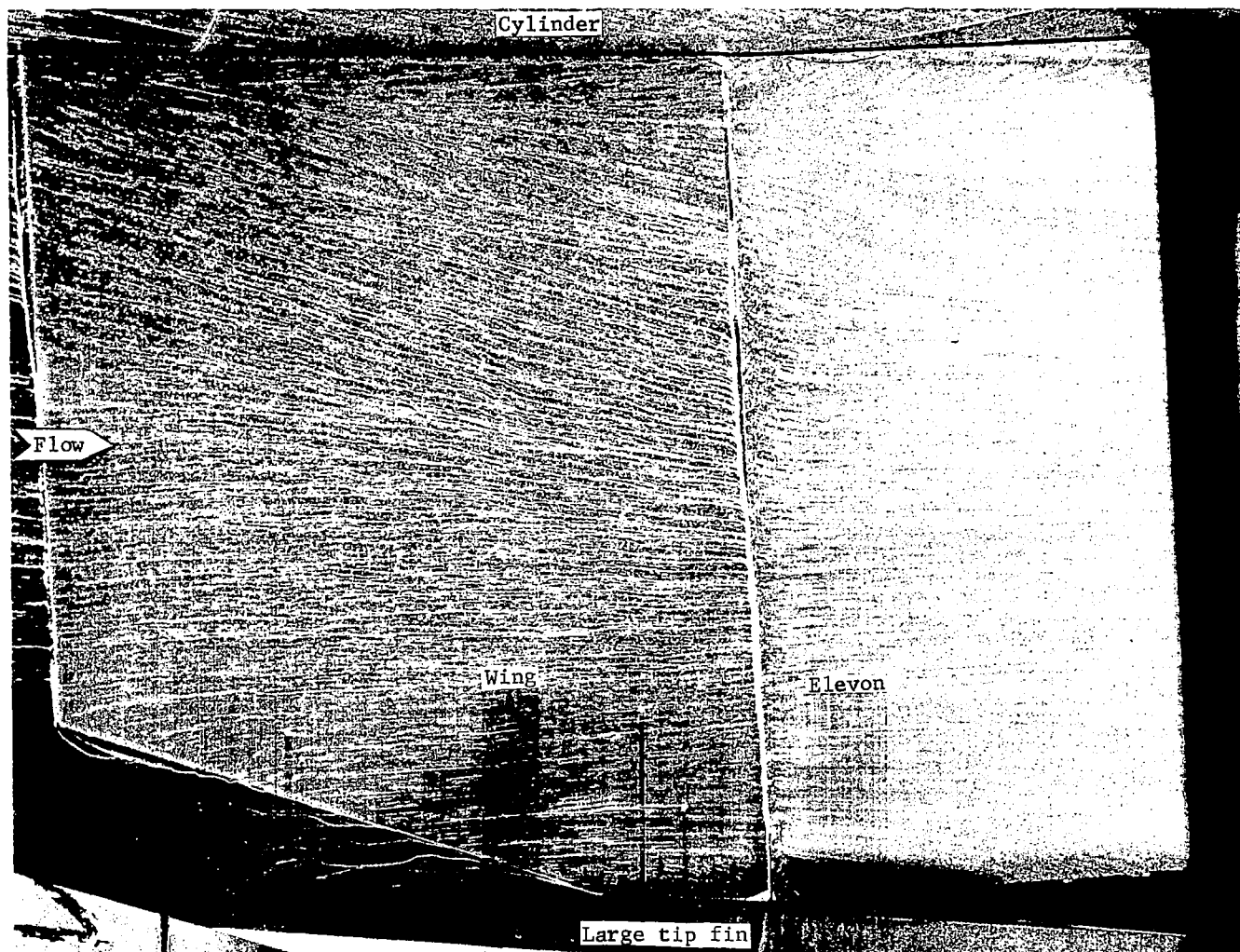


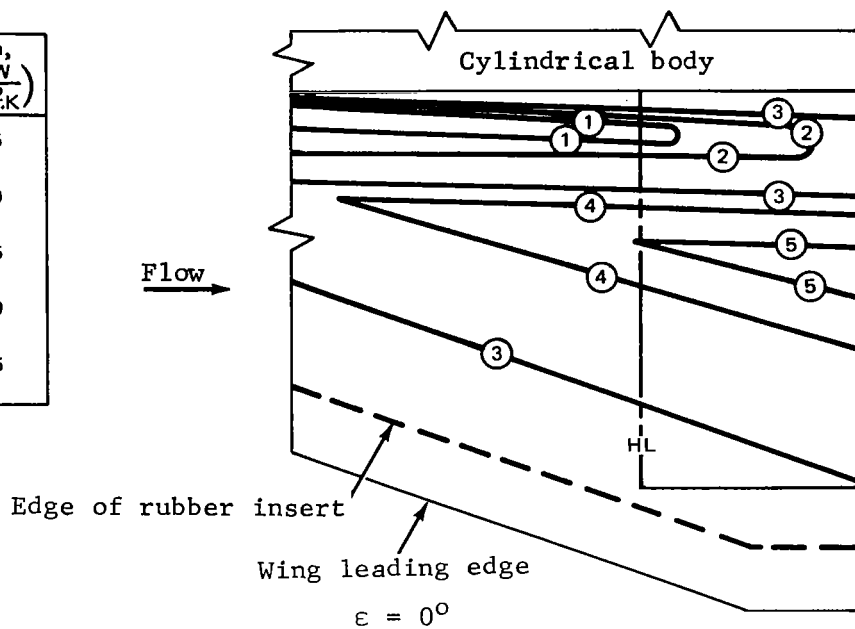
Figure 29.- Large distortion in oil accumulation line upstream of 30° elevon on 70° swept wing when end plate is replaced by cylindrical body.



L-78-169

Figure 30.- Frame from planform oil-flow motion picture showing wing and elevon surfaces;  
 $\epsilon = 20^\circ$ ,  $\Lambda = 70^\circ$ , cylindrical body and large tip fin attached.

Con- tour	$\left(\frac{h}{W}\right)$ $\left(\frac{1}{m^2 \cdot K}\right)$
①	135
②	110
③	85
④	70
⑤	65



Con- tour	$\left(\frac{h}{W}\right)$ $\left(\frac{1}{m^2 \cdot K}\right)$
①	650
②	350
③	130
④	90
⑤	75

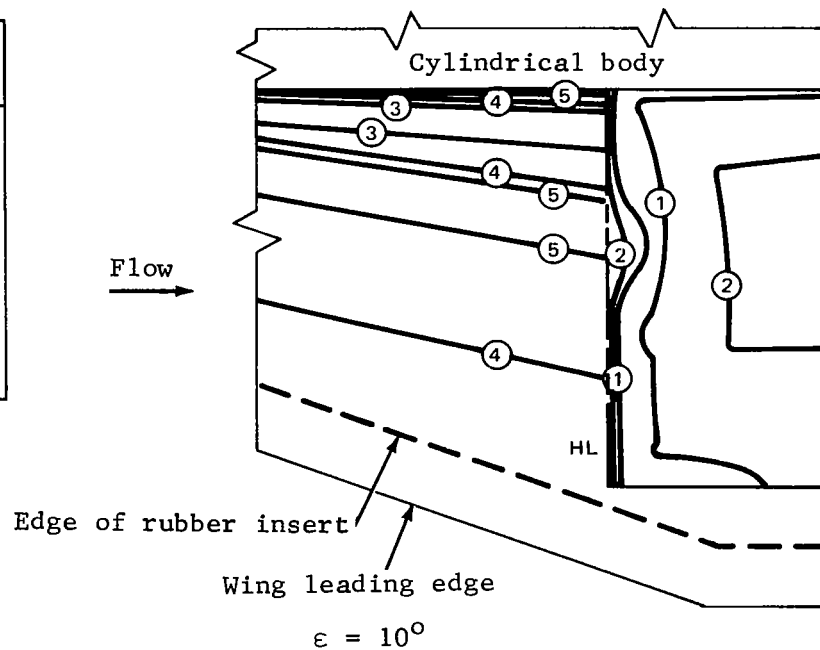


Figure 31.- Cylindrical-body effects on contours of constant heat-transfer-rate coefficients on 70° wing and elevon surfaces for  $\epsilon = 0^\circ$  and  $10^\circ$ .

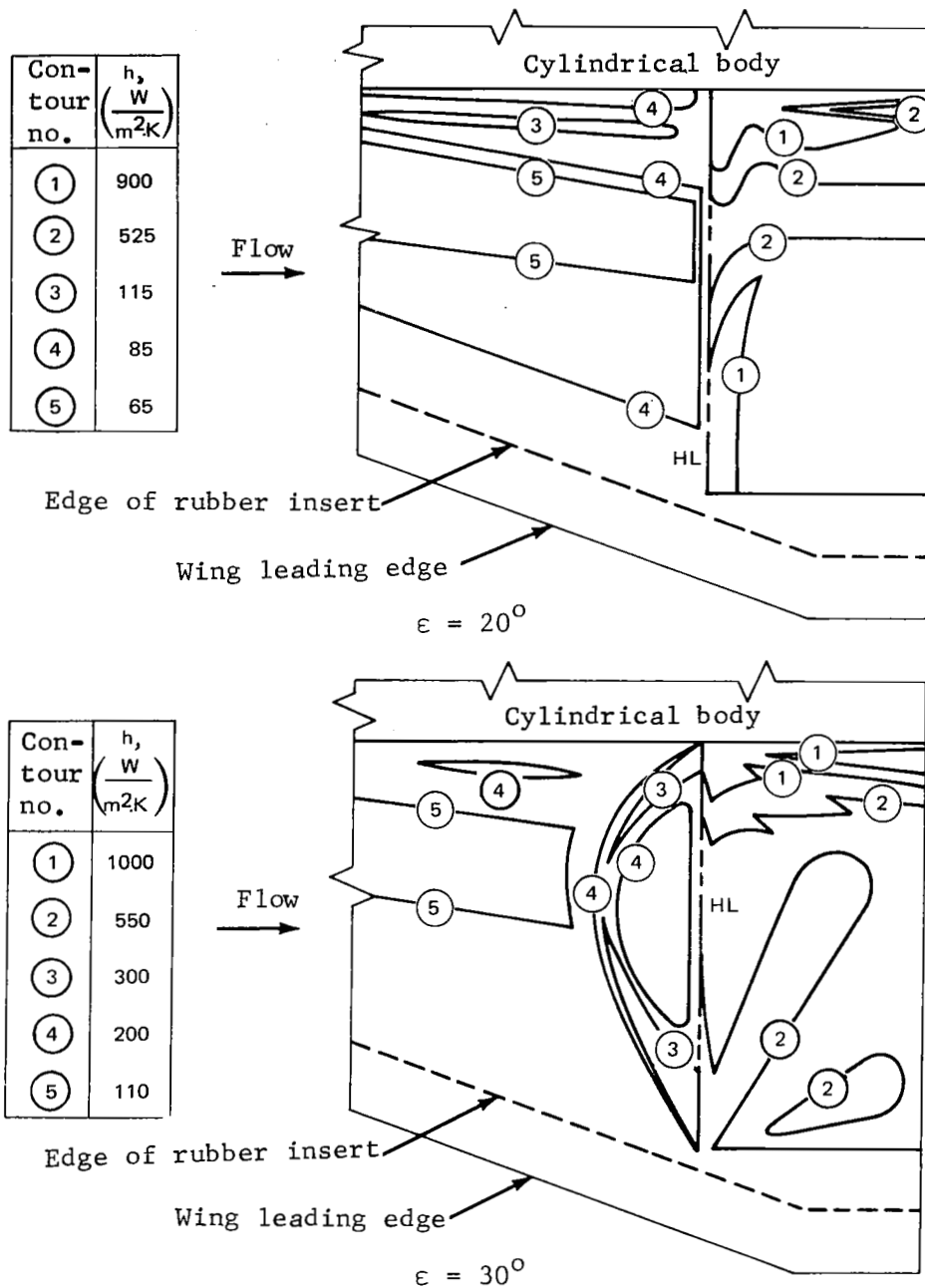


Figure 32.- Cylindrical-body effects on contours of constant heat-transfer-rate coefficients on  $70^\circ$  wing and elevon surfaces for  $\epsilon = 20^\circ$  and  $30^\circ$ .

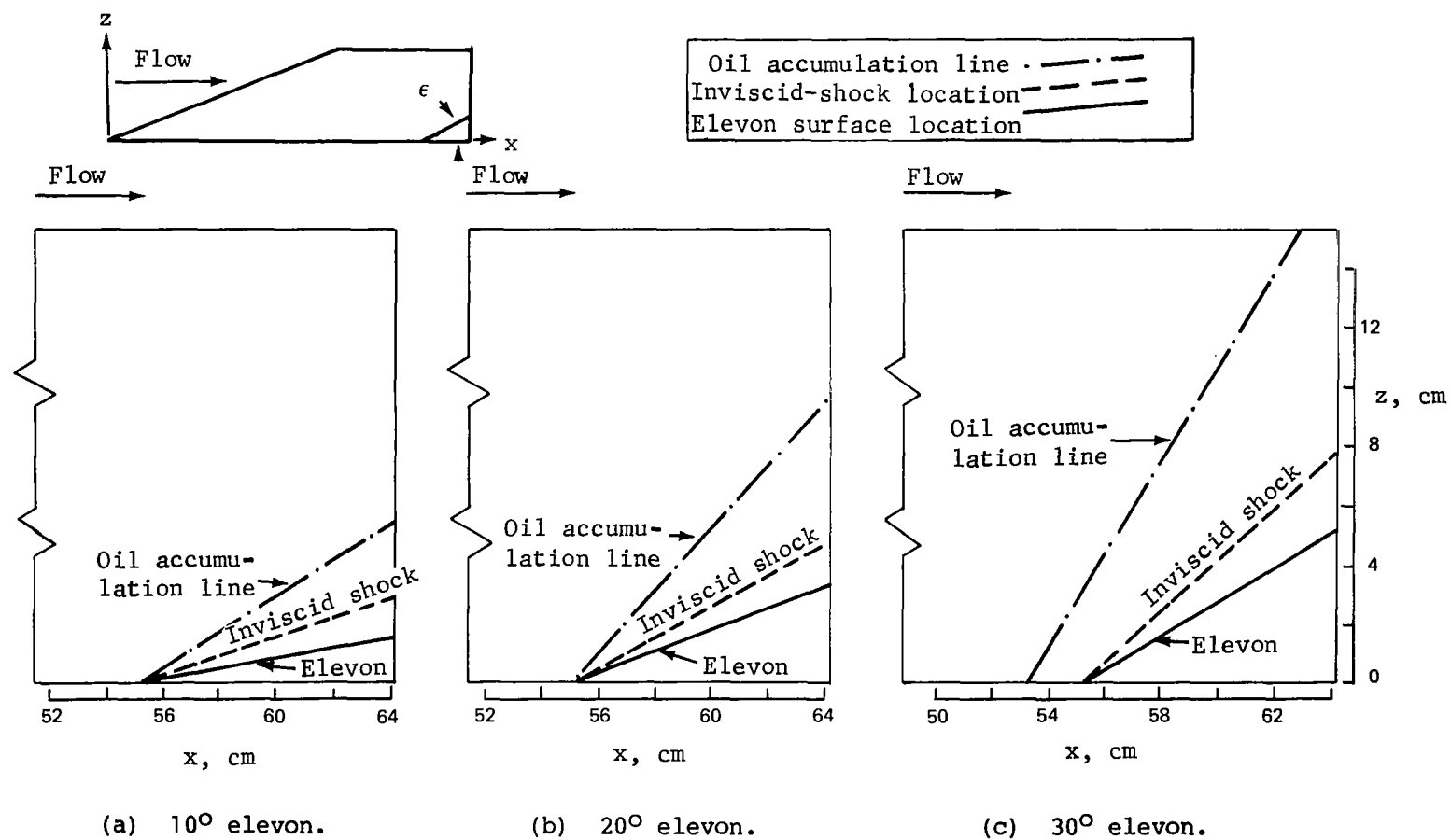


Figure 33.- Oil accumulation lines and inviscid-flow shock-wave locations on end-plate surface for various elevon deflection angles;  $\Lambda = 0^\circ, 50^\circ, \text{ or } 70^\circ$ .

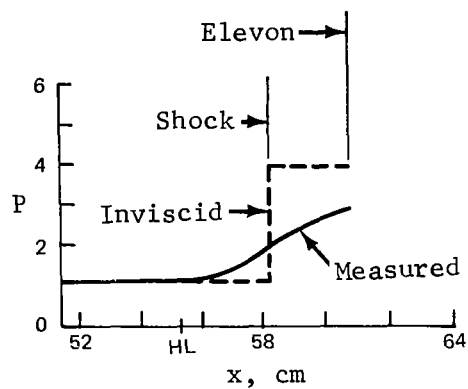
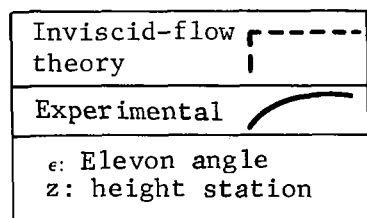
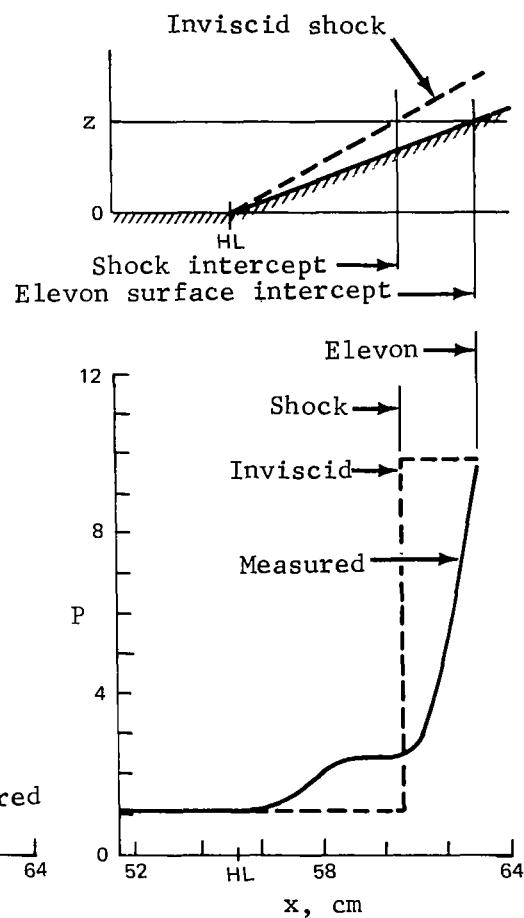
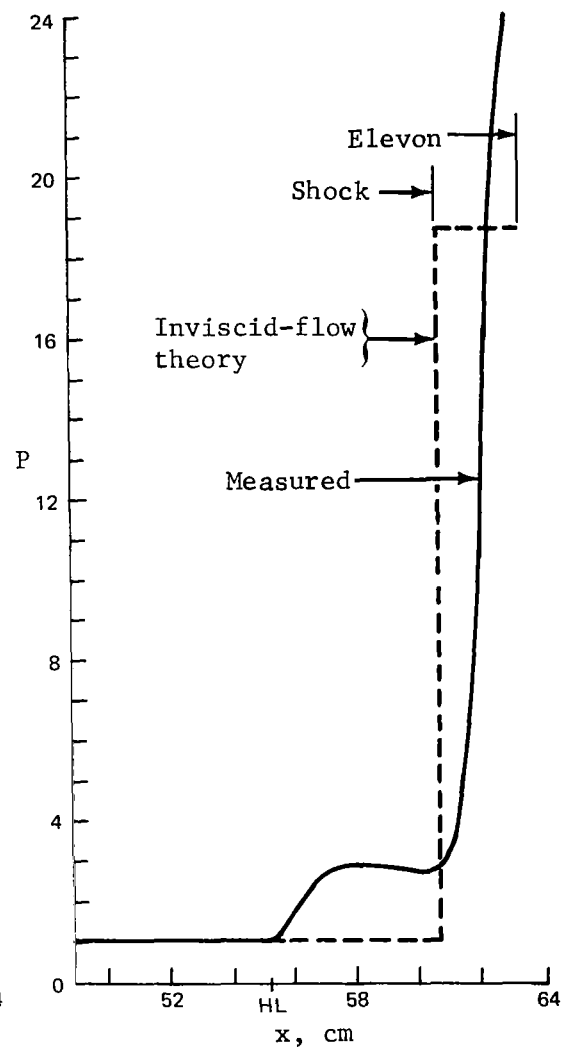
(a)  $\epsilon = 10^\circ$ ,  $z = 0.95$  cm.(b)  $\epsilon = 20^\circ$ ,  $z = 2.86$  cm.(c)  $\epsilon = 30^\circ$ ,  $z = 4.76$  cm.

Figure 34.- Streamwise pressure-ratio distributions on end-plate surface;  $\Lambda = 0^\circ$ ,  $50^\circ$ , or  $70^\circ$ .



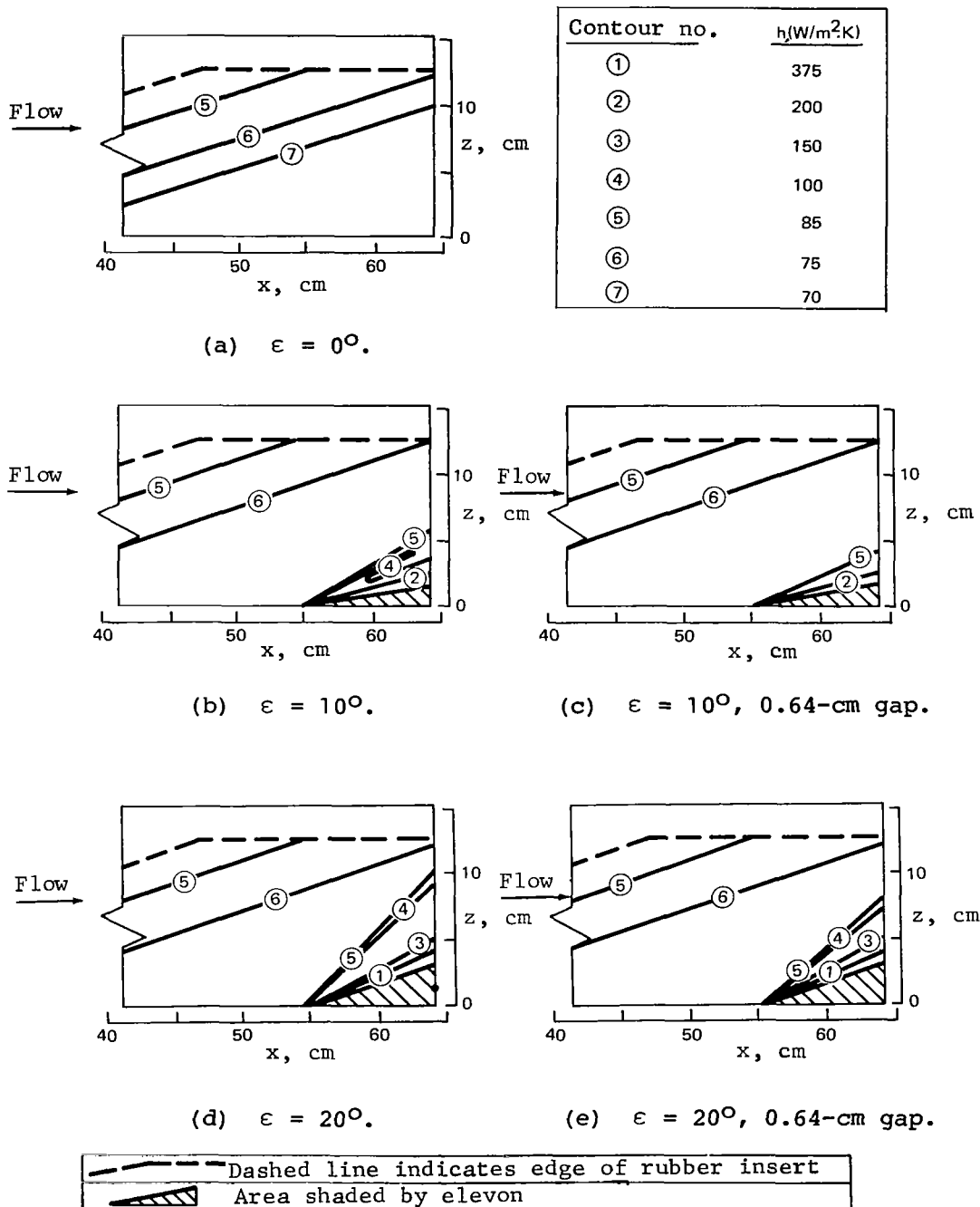
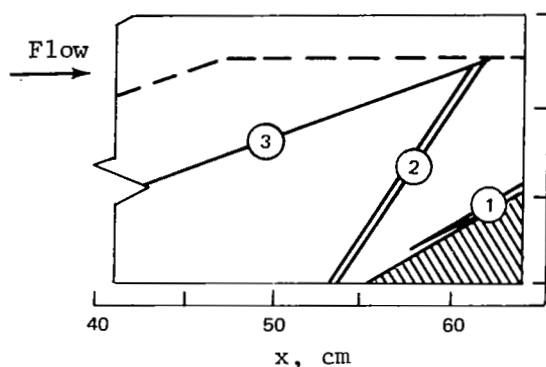
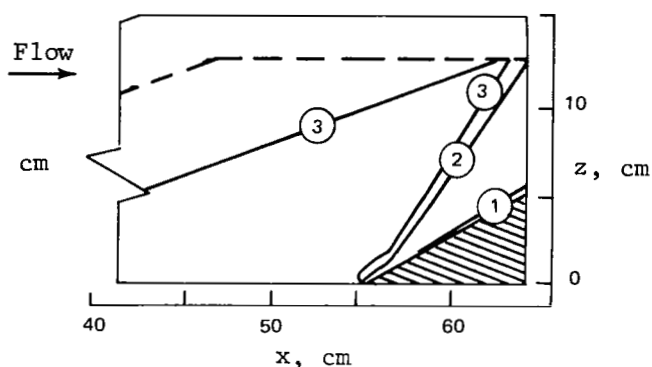


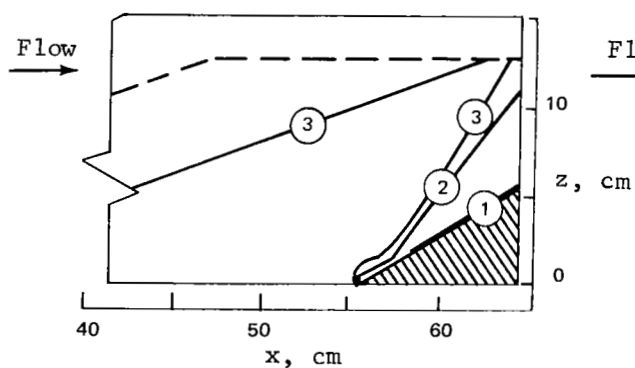
Figure 35.- Contours of constant heat-transfer-rate coefficients on end-plate surface for  $\epsilon = 0^\circ, 10^\circ$ , and  $20^\circ$ ;  $\Lambda = 0^\circ, 50^\circ$ , or  $70^\circ$ .



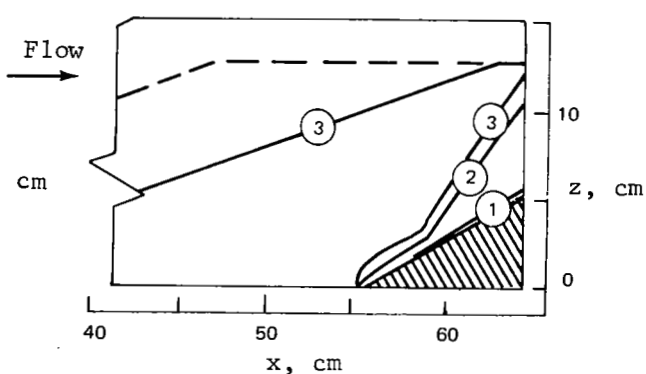
(a) No gap.



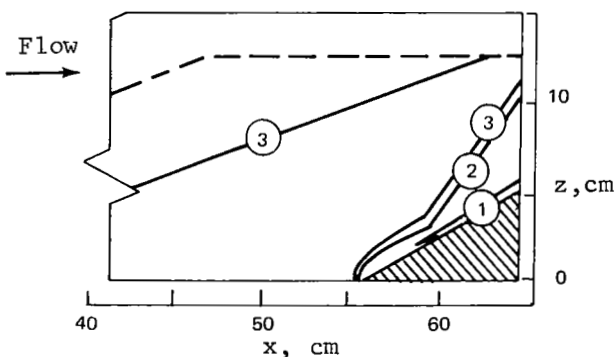
(b) 0.32-cm gap.



(c) 0.64-cm gap.



(d) 0.95-cm gap.



(e) 1.27-cm gap.

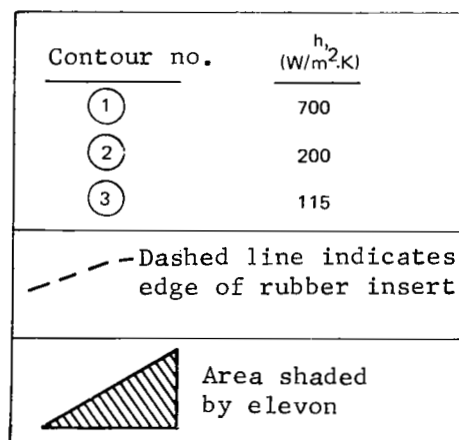


Figure 36.- Contours of constant heat-transfer-rate coefficient on end-plate surface for  $\epsilon = 30^\circ$ ;  $\Lambda = 0^\circ, 50^\circ, \text{ or } 70^\circ$ .

1. Report No. NASA TP-1356		2. Government Accession No.		3. Recipient's Catalog No.	
4. Title and Subtitle PRESSURE AND THERMAL DISTRIBUTIONS ON WINGS AND ADJACENT SURFACES INDUCED BY ELEVON DEFLECTIONS AT MACH 6				5. Report Date March 1979	
				6. Performing Organization Code	
7. Author(s) Louis G. Kaufman II and Charles B. Johnson				8. Performing Organization Report No. L-12636	
9. Performing Organization Name and Address  NASA Langley Research Center Hampton, VA 23665				10. Work Unit No. 505-11-31-02	
				11. Contract or Grant No.	
12. Sponsoring Agency Name and Address  National Aeronautics and Space Administration Washington, DC 20546				13. Type of Report and Period Covered Technical Paper	
				14. Sponsoring Agency Code	
15. Supplementary Notes  Louis G. Kaufman II: Grumman Aerospace Corp., Bethpage, New York. Charles B. Johnson: Langley Research Center.					
16. Abstract  Surface pressure distributions and heat transfer distributions were obtained on wing half-models in regions where three-dimensional separated-flow effects are prominent. Unswept and 50°- and 70°-swept semispan wings were tested, for trailing-edge-elevon ramp angles of 0°, 10°, 20°, and 30°, with and without cylindrical and flat-plate center bodies and with and without various wing-tip plates and fins. The data, obtained for a free-stream Mach number of 6 and a wing-root-chord Reynolds number of $18.5 \times 10^6$ , reveal considerably larger regions of increased pressure and thermal loads than would be anticipated using non-separated flow analyses.					
17. Key Words (Suggested by Author(s))  Turbulent boundary layer Hypersonic flow Viscid-inviscid action Flow separation Pressure distributions Heat transfer			18. Distribution Statement  Unclassified - Unlimited   Subject Category 34		
19. Security Classif. (of this report) Unclassified	20. Security Classif. (of this page) Unclassified	21. No. of Pages 56	22. Price* \$5.25		

\* For sale by the National Technical Information Service, Springfield, Virginia 22161

NASA-Langley, 1979

National Aeronautics and  
Space Administration

Washington, D.C.  
20546

Official Business

Penalty for Private Use, \$300

THIRD-CLASS BULK RATE

Postage and Fees Paid  
National Aeronautics and  
Space Administration  
NASA-451



2 1 10, D, 022379 S00903DS  
DEPT OF THE AIR FORCE  
AF WEAPONS LABORATORY  
ATTN: TECHNICAL LIBRARY (SUL)  
KIRTLAND AFB NM 87117

**NASA**

POST

**S**

Deliverable (Section 158  
Manual) Do Not Return